Role of the crystal chemistry on the dissolution kinetics of Fe(III)-rich smectites

Delphine Masson, Valentin Robin, Emmanuel Joussein, Emmanuel Tertre, Fabien Baron

To cite this version:

Delphine Masson, Valentin Robin, Emmanuel Joussein, Emmanuel Tertre, Fabien Baron. Role of the crystal chemistry on the dissolution kinetics of Fe(III)-rich smectites. Geochimica et Cosmochimica Acta, 2024, 371, 10.1016/j.gca.2024.01.028 . hal-04442866

HAL Id: hal-04442866
https://hal.science/hal-04442866v1

Role of the crystal chemistry on the dissolution kinetics of Fe(III)-rich smectites

D. Masson[1], V. Robin[1], E. Joussein[1], E. Tertre[2] & F. Baron[2]

[1]*Université de Limoges, E2Lim UR 24133, 123 av. A. Thomas, 87060 Limoges Cedex, France*

[2]*Université de Poitiers, IC2MP UMR CNRS 7285, 4 rue M. Brunet, 86022 Poitiers Cedex, France*

Abstract

Smectites are reactive minerals that are present in surface environments. Most of the smectite dissolution kinetics reported in the literature are related to Al-rich smectites, whereas Fe(III)-rich smectites, which are commonly found in soils, have not been well studied. In this study, the impact of structural Fe(III) in smectites on the dissolution kinetics is determined under acidic conditions. The dissolution kinetics of three pure Fe(III)-rich smectites with different crystal chemistries $(Si_{7.16}Fe^{3+}_{0.84})(Fe^{3+}_{3.46}Mg_{0.54})O_{20}(OH)_4Na_{1.38}$, $(Si_{6.86}Fe^{3+}_{1.14})(Fe^{3+}_{4})O_{20}(OH)_4Na_{1.14}$, and $(Si_{7.34}Fe^{3+}_{0.66})(Fe^{3+}_{4})O_{20}(OH)_4Na_{0.66}$) are investigated at 25°C using flow-through experiments at pH values between 1.8 and 5.5. The measured dissolution rates are compared with published rates for Al-rich smectites. The concentrations of dissolved Si, Fe and Mg are measured as a function of time, and the retrieved residual solids are analyzed via infrared spectroscopy and transmission electron microscopy. The steady-state dissolution rates of the synthetic smectites calculated from the amount of Si release (R_{Si}) decrease with increasing pH. A comparison of the dissolution rates as a function of pH does not allow us to observe major effects of the crystal chemistry among the synthetic smectites. However, the dissolution rates calculated for synthetic Fe(III)-rich smectites are systematically greater than those of Al-rich smectites. The measured dissolution rates decrease as the aqueous system approaches equilibrium. Different behaviors are observed for Fe(III)-rich (i.e., > 4

Fe(III)/$O_{20}(OH)_4$) and Al-rich smectites as the $R_{Si}=f(\Delta G)$ functions differ, with Fe(III)-rich smectites exhibiting greater instability than Al-rich smectites. Under the most acidic conditions investigated (pH 1.8 and 2), the crystal chemistry and mineralogy of the smectite changed during dissolution, with a relatively greater loss of tetrahedral Fe than of octahedral Fe and the formation of amorphous silica phases. These results show that the amount and location of structural Fe(III) in smectites impact the stability of the minerals. This suggests that the dissolution rate of smectites as a function of the ionic activity product classically used to describe reactive transport should consider the effects of the crystal chemistry, in particular, the amount of structural Fe(III), which is rather high, especially in soil smectites.

Key words: smectite, crystal chemistry, structural Fe(III), dissolution kinetics, acidic conditions

Introduction

Smectites are ubiquitous in surface environments and are commonly present in the fine fraction (<2 µm) of soils and sediments. In these environments, smectite particles can be very small (i.e., <0.2 µm) (Laird et al., 1991), with high specific surface areas (e.g., >600 m^2 g^{-1}) and cation exchange capacity (CEC; e.g., > 80 $cmol_{(+)}$ kg^{-1}). As a result, smectites in soils and sediments are responsible for most of the capacity to retain cations in these environments (Hubert et al., 2012; Viennet et al., 2015; Martin et al., 2018; Bakker et al., 2018, 2019) and play a key role in the mobility of nutrients and contaminants in these systems (Chorover and Amistadi, 2001; Haack et al., 2008; Vorhies and Gaines, 2009; Ferret et al., 2014; Parrello et al., 2016; Robin et al., 2020).

Smectites are 2:1 swelling clays whose layers are composed of one octahedral sheet sandwiched between two tetrahedral sheets. In dioctahedral smectites, the octahedral sheet is mainly occupied by trivalent cations (i.e., aluminum (Al) or ferric iron [Fe(III)]), whereas the tetrahedral sheets are mainly composed of tetravalent silicon (Si). Heterovalent substitutions commonly occur in both the tetrahedral (e.g., Al(III) or Fe(III) for Si(IV) substitutions) and octahedral (e.g., magnesium Mg(II) for Al(III) or Fe(III) substitutions) sheets. The net negative charge of the smectite layers generated by these substitutions is compensated for by the incorporation of cations in the interlayer space. Depending on the nature of the main cations in the octahedral sheet and the location of the main negative charge in the structure (tetrahedral or octahedral), smectites can be defined as beidellite (Al-rich smectite with a predominant tetrahedral charge), nontronite (Fe(III)-rich smectite with a predominant tetrahedral charge), or montmorillonite (Al-rich smectite with a predominant octahedral charge). Note that soil smectites are typically characterized by a rather high structural charge ($>0.45/O_{10}(OH)_2$), a high tetrahedral charge, and a high Fe(III) content in the octahedral sheet (Tessier and Pédro, 1985; Stucki et al., 1987). Fe-rich clays are ubiquitous minerals in soils, and Fe-rich beidellite is commonly present (Stucki et al., 1987; Badraoui and Bloom, 1990; Wilson, 1999). As a consequence, the properties of Fe-rich smectites play important roles in the chemical and physical properties of soils.

In the literature, discussions of the stability of smectites have focused on the kinetic dissolution of bentonites (i.e., materials composed of montmorillonites) due to their excellent application potential in the context of the long-term behavior of engineered clay barriers used for nuclear waste storage (Marty et al., 2011; Kaufhold et al., 2019; Jalal et al., 2021) or chemical and pharmaceutical applications (Jayrajsinh et al., 2017; França et al., 2022). Numerous flow-through experiments have been performed to assess the effects of environmental parameters, such as pH (Metz et al., 2005; Amram and Ganor, 2005; Rozalén et al., 2008; Cappelli et al., 2018), temperature (Amram and Ganor, 2005; Rozalen et al., 2009; Marty et al., 2011), ionic strength and the presence of soluble organic acids (Golubev et al., 2006; Ramos et al., 2011, 2014), on the constant dissolution rate of montmorillonites. However, studies that have focused on the kinetics of the Fe-rich smectites commonly found in soils are limited. Gainey et al. (2014) studied the dissolution rate of a natural nontronite (Nau-1 from the Clay Minerals Society) and showed a faster dissolution rate for nontronite than for beidellite (SBId-1 from the Clay Minerals Society) despite the similarity in particle sizes and total layer charges between the two minerals. Thus, the role of the crystal chemistry (i.e., the amount, nature and location of charge) on the dissolution kinetics of Fe-rich smectites has not been studied in detail.

Smectites are commonly mixed with nonclayey minerals in natural samples and/or are interstratified mixed-layer minerals (see discussion in Hubert et al., 2012). Therefore, using natural samples to assess the role of the structural Fe content, structural charge and location of the charge (tetrahedral or octahedral) on the stability of these minerals is not trivial. To overcome this difficulty, a synthesis approach (Baron et al., 2016; Petit et al., 2017) enabling us to control the crystal chemistry of Fe(III)-smectites was applied in this study. The hydrothermal sol-gel synthesis used here allowed us to prepare synthetic particles with a high proportion of Fe(III) and a size comparable to that of soil particles (<100 nm) and to control the amount and location of heterovalent substitutions. The dissolution kinetics of three synthetic Fe(III)-rich smectites, differing in terms of the content and location of structural Fe(III) (tetrahedral vs. octahedral), were studied using flow-through reactors at pH (HNO_3) values between 1.8 and 5.5. The concentrations of Si, Fe, and Mg in solution were analyzed as a function of time and used to calculate the dissolution rates and to elucidate the mechanisms associated with dissolution. Both aqueous concentration measurements and solid-state analysis (FTIR and TEM) allowed us to interpret the effects of crystal chemical parameters on the reactivity of the three Fe(III)-rich smectites at acidic pH. A comparison with published data obtained for smectites with distinct crystal chemistry allowed us to discuss the effect of structural Fe(III) (i) on the stability of these minerals and (ii) for further reactive modelling approach involving smectite data.

2. Materials and methods

2.1. Synthetic smectites

2.1.1. Synthesis

Three Fe(III)-rich smectites were synthesized that differ in terms of their heterovalent substitutions, i.e., (i) their amount (permanent layer charge from 0.66 to 1.38 per unit cell) and (ii) their location in the smectite layer (only in tetrahedral sites or in both tetrahedral and octahedral sites). Syntheses were performed according to the procedures described by Baron et al. (2016) and Petit et al. (2017) using a precursor gel obtained by coprecipitation of sodium metasilicate, ferric iron chloride, and magnesium chloride solutions. After precipitation, each precursor gel was collected by filtration at 0.45 µm and placed in a PTFE metallic-coated hydrothermal reactor. The amount of Fe(III) for Si(IV) tetrahedral substitutions was controlled by the addition of 0.02 M NaOH solution to adjust the pH (Baron et al., 2016; Petit et al., 2017). Magnesium chloride was added to introduce octahedral substitutions (Mg(II) for Fe(III)). The hydrothermal synthesis was conducted at 150°C for 7 days. Then, the solid materials were recovered by filtration at 0.1 µm, dispersed in a 2 M NaCl solution to achieve Na saturation and rinsed by dialysis to remove the excess salt before being stored as a suspension prior to the dissolution experiments.

2.1.2. Solid analysis

Infrared (FTIR) analyses were performed to assess the changes in the crystal chemistry in the clay minerals after dissolution and the neoformation of any IR-sensitive minerals. FTIR spectra were obtained in transmission mode at a resolution of 4 cm^{-1} in the mid-infrared (MIR) range (4000-400 cm^{-1}) using a Thermo Scientific Nicolet iS50 FTIR spectrometer equipped with a KBr beam splitter, an Ever-Glo source, and a DTGS-KBr detector. MIR spectra were collected from KBr pellets (obtained by mixing 1 mg of sample with 150 mg of KBr) which were pressed in a 10 mm diameter press die for 5 min at 8 kbar and dried for 1 day at 110°C.

Transmission electron microscopy (TEM) and high-resolution transmission electron microscopy (HRTEM) were performed with a Jeol 2100 UHR (LaB6) transmission electron microscope at 200 kV in conjunction with energy dispersive X-ray spectroscopy (EDS) to observe the particle morphology and structural organization and to perform local chemical analysis. The samples were dispersed in deionized water using sonication, and a droplet of the suspension was then placed on a TEM copper grid and dried at ambient temperature.

2.1.3. Description of the three synthetic Fe(III)-rich smectites

Preliminary results obtained using infrared spectroscopy and X-ray diffraction (XRD) confirmed the synthesis of 2:1 swelling clay minerals without other detectable mineral phases: neither amorphous silica nor other impurities were formed (see Figs. S1 and S2 and the associated discussion in the supplementary material). The structural formulas of the initial synthetic Fe(III)-rich smectites were determined by either FTIR spectroscopy (Baron et al., 2016) or EDS with scanning electron microscopy (SEM), and the results are reported in Table 1. SEM-EDS analyses were performed on pressed disks (7 mm) of pure synthetic particles. Chemical analyses of individual particles were also performed using TEM-EDS to evaluate the homogeneity of the synthetic Fe(III)-rich smectites.

Chemical analyses via either SEM or TEM showed that the synthetic smectite particles were homogeneous. Fe(III)-rich smectites are named according to their crystal chemical properties; i.e., Sm-LC, Sm-HC and Sm-Mg indicate low-charge smectite, high-charge smectite and Mg(II) for Fe(III) substitutions smectite, respectively.

The structural formulas of Sm-HC and Sm-LC show that the net negative permanent layer charge (100%) originated from Fe(III) substitutions for Si(IV) in the tetrahedral sheets, whereas for Sm-Mg, the negative charge was distributed between the tetrahedral (61% Fe(III) for Si(IV)) and octahedral (39%) sheets due to Mg(II) substitutions for Fe(III) (Table 1). Sm-HC and Sm-Mg exhibited high permanent layer charges of 1.14 and 1.38 per unit formula, respectively, while the permanent layer charge was only 0.66 for Sm-LC (Table 1). The size of the synthetic smectite particles was fairly homogeneous and was estimated to be approximately 100 nm using TEM observations.

2.2. Flow-through experiments

Fifteen dissolution experiments were performed using flow-through reactors with input acidic solutions (pH between 1.80 and 5.50) prepared using a 69% HNO_3 (AR grade) solution and Milli-Q water. $NaNO_3$ salt (AR grade) was added to the input solutions as a background electrolyte to achieve ionic strength of 10^{-3} M. Given the small size of the synthetic particles, to avoid membrane clogging or loss of particles from the reactor, two open reactor types were used according to the approach proposed by Köhler et al. (2005) (Fig. 1). The first type of reactor (Fig. 1A) consisted of a PTFE cell with a total volume of 30 mL. The input solution was in contact with the smectite particles. The suspension in the system was homogenized by continuous stirring with a suspended Teflon-coated magnetic bar. The outlet solution was filtered through a 0.22 µm PVDF membrane.

Table 1. Details related to the structural formula of the three synthetic Fe(III)-rich smectites.

Structural formulas of synthetic Fe(III)-rich smectites	**Global charge (per $O_{20}(OH)_4$)**	**Nature and % tetrahedral charge**	**Nature and % octahedral charge**	**Tetrahedral Si/Fe ratio**	**Global Si/Fe ratio**

Sm-HC	1.14	Fe (III) → Si	0	6.02	1.33
$(Si_{6.86}Fe^{3+}_{1.14})(Fe^{3+}_{4})O_{20}(OH)_{4}Na_{1.14}$		100			
Sm-LC	0.66	Fe (III) → Si	0	11.12	1.58
$(Si_{7.34}Fe^{3+}_{0.66})(Fe^{3+}_{4})O_{20}(OH)_{4}Na_{0.66}$		100			
Sm-Mg	1.38	Fe (III) → Si	Mg → Fe (III)	8.52	1.66
$(Si_{7.16}Fe^{3+}_{0.84})(Fe^{3+}_{3.46}Mg_{0.54})O_{20}(OH)_{4}Na_{1.38}$		61	39		

The second type of reactor (Fig. 1B) consisted of a 180 mL polycarbonate column. Smectite particles were enclosed in a dialysis bag with a 7000 Dalton (≃ 1.5 nm) pore size. The dialysis bag was sealed tightly and placed inside the column in contact with the input solution. In the type B reactor, the fluid was mixed by placing the columns on an oscillating shaker. Table S1 lists the experimental conditions.

All the experiments were performed at 20±1°C in a temperature-controlled room. The flow rate of the input solution was set at $1.07\times10^{-3} \pm 6.00\times10^{-5}$ for type A reactors or $7.68\times10^{-4} \pm 2.20\times10^{-5}$ $mL.s^{-1}$ for type B reactors using an Ismatec® peristaltic pump. Since steady-state dissolution of clay minerals may not occur (Kohler et al., 2005), we proposed that a steady state was achieved when the output Si concentration remained approximately constant, i.e., differing by less than 6% across six consecutive samples collected every 24 h, as proposed in previous studies (Rozalén et al., 2008; Robin et al., 2016; Cappelli et al., 2018).

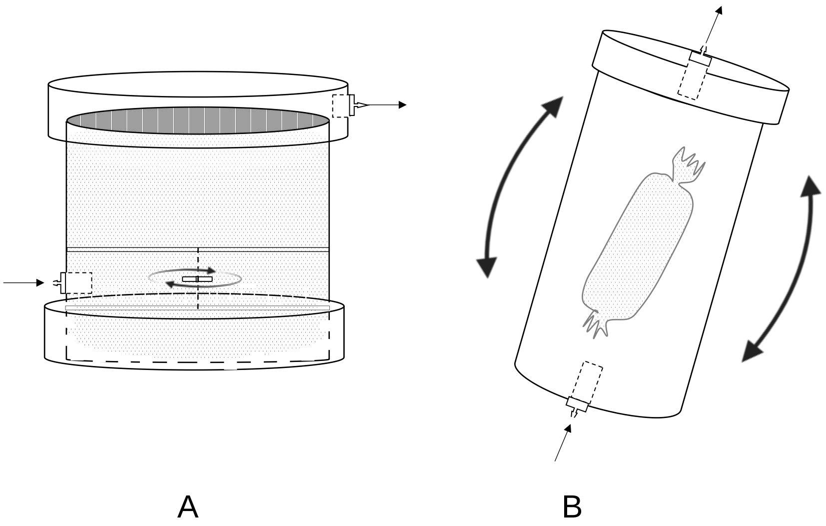

Fig. 1. Schematic illustration of the two types of reactors (A and B) used in this study. Reactor B was adapted from Kohler et al. (2005).

2.3. Solution analysis

Output solutions were collected every day or every two days. The collected solutions were analyzed for pH, oxidation potential (ORP) and total aqueous Si, Fe, and Mg concentrations. The pH was measured immediately after sample collection using precalibrated pH combination electrode (Accumet® 13-620-AE6). A WTW-SenTix® ORP electrode standardized with an ORP test solution (240 mV) was used to measure the ORP. The Si, Fe and Mg concentrations were determined for acidified samples (2% HNO_3 v/v).

At pH 1.80 and 2, the aqueous concentrations of Si, Fe and Mg were determined via microwave plasma-atomic emission spectroscopy (MP-AES, Agilent MP 4100). The limits of quantification were 2.71 µM, 1.27 µM and 0.5 µM for Si, Fe, and Mg, respectively. For samples collected between pH 3 and 5.5, the aqueous Si concentration was determined by colorimetry using the molybdate blue method (Strickland and Parsons, 1972), and the absorbance at 810 nm was measured in 5 cm cells with a Shimadzu UV-1800 UV-Vis spectrophotometer. The limit of quantification was 0.02 µM. Aqueous Fe and Mg concentrations were measured using inductively coupled plasma mass spectrometry (Agilent Technology 7700× ICP-MS from Santa Clara, CA, USA) using ^{45}Sc and ^{115}In as internal standards. The limits of quantification were 0.03 µM for Fe and Mg.

2.4. Calculations

Dissolution rate. The steady-state dissolution rate R (mol g^{-1} s^{-1}) was calculated from aqueous Si (or Fe) concentrations by using the following equation (Metz et al., 2005):

$$R_j = \frac{-1}{\nu_j} \frac{q}{m} C_j \quad (1)$$

where ν is the stoichiometric coefficient of component *j* (i.e., Si or Fe) in the dissolution reaction, *q* is the flow rate (L s^{-1}), *m* is the sample mass (g) (obtained by subtracting the amount of dissolved element from the initial amount of sample), and *C* is the concentration of component *j* (i.e., Si or Fe) in the output solution (mol L^{-1}).

A common practice in some experimental dissolution kinetics studies of clay minerals is to normalize the dissolution rate to their specific surface areas (e.g., either partial or total surface including interlayer, external surface or edge surface; Metz and Ganor, 2001; Cama et al., 2002; Bibi et al., 2011; Daval et al., 2013). However, several studies on phyllosilicates (and with silicates in general) revealed that dissolution reactions at different specific sites (e.g., etch-pits opening on basal surfaces or edge retreat) may differ, indicating that reactive and overall surface areas are not equivalent (Grybos et al., 2010; Cappelli et al., 2020; N'Guessan et al., 2021). As the relative reactivity of each surface type remains unknown, the dissolution rates of smectites were normalized in the present study to the mass, as proposed by Metz et al. (2005), Amram and Ganor (2005), Robin et al. (2016) and Cappelli et al. (2018) (among others); this choice allowed us to compare the dissolution rates of smectites or other phyllosilicates (Marty et al., 2005; Rozalén et al., 2008) without being impacted by the choice of surface normalization. The propagated error associated with the calculated dissolution rate was estimated according to the Gaussian error propagation method for independent variables (Wells and Krakiwsky, 1971). The error in the calculated rate was less than 5% and was dominated by the uncertainty in the measured Si (or Fe) concentration in the output solution.

Thermodynamic calculations. PHREEQC software version 4 (Parkhurst and Appelo, 1999) and the Thermoddem thermodynamic database (Blanc et al., 2012) were used to calculate the aqueous speciation and the saturation state of the output solutions.

The saturation indexes (SI) of the output solutions with respect to the phases of interest were calculated using the ion activity product (IAP) of the solution and the equilibrium constant (K_{eq}) (2).

$$SI = log\frac{IAP}{K_{eq}} \qquad (2)$$

The dissolution K_{eq} values of the three synthetic Fe(III)-rich smectites at 25°C and 1 atm were computed according to the method proposed by Blanc et al. (2021) (a brief description of this approach is provided in the supplementary material) according to the following dissolution reactions:

$(Si_{6.86}Fe(III)_{1.14})(Fe(III)_4)O_{20}(OH)_4Na_{1.14\,(s)} + 16.56H^+ + 3.44\,H_2O \rightarrow 5.14Fe^{3+}{}_{(aq)} + 6.86H_4SiO_{4(aq)} + 1.14Na^+{}_{(aq)}$

Log K_{eq} = -9

$(Si_{7.34}Fe(III)_{0.66})(Fe(III)_4)O_{20}(OH)_4Na_{0.66(s)} + 14.64H^+ + 5.36\,H_2O \rightarrow 4.66Fe^{3+}{}_{(aq)} + 7.34H_4SiO_{4(aq)} + 0.66Na^+{}_{(aq)}$

Log K_{eq} = -10.07

$(Si_{7.16}Fe(III)_{0.84})(Fe(III)_{3.46}Mg_{0.54})O_{20}(OH)_4Na_{1.38(s)} + 15.36H^+ + 4.64H_2O \rightarrow 4.30Fe^{3+}{}_{(aq)} + 7.16H_4SiO_{4(aq)} + 0.54Mg^{2+}{}_{(aq)} + 1.38Na^+{}_{(aq)}$

Log K_{eq6} = -2.55

The degree of saturation of the output solutions with respect to the different smectites was calculated in terms of the Gibbs free energy of reaction Δ_rG (in kcal mol^{-1}), which was defined as

$$\Delta G_r = RTln\left(\frac{IAP}{K_{eq}}\right) \qquad (3)$$

where R is the gas constant (8.314 J mol^{-1} K^{-1}) and T is the absolute temperature (K).

3. Results

3.1. Output solution analysis

Good reproducibility of the dissolution rates was achieved between experiments performed with the two reactor types under the same conditions (pH, starting material). The differences between the experimental dissolution rates obtained with reactor A and reactor B varied from 3% to 12% (Table S1). These differences are acceptable and allowed a comparison of the results regardless of the reactor used.

Fig. 2 shows the output Si, Fe and Mg concentrations and the aqueous Si/Fe and solid Si/Fe stoichiometric ratios for the three samples at pH 1.8, 2 and 3. The results of the experiments performed at pH 4 and 5 are shown only for LC smectite (representative experiments). The data obtained under other experimental conditions are reported in Fig. S3 (supplementary material).

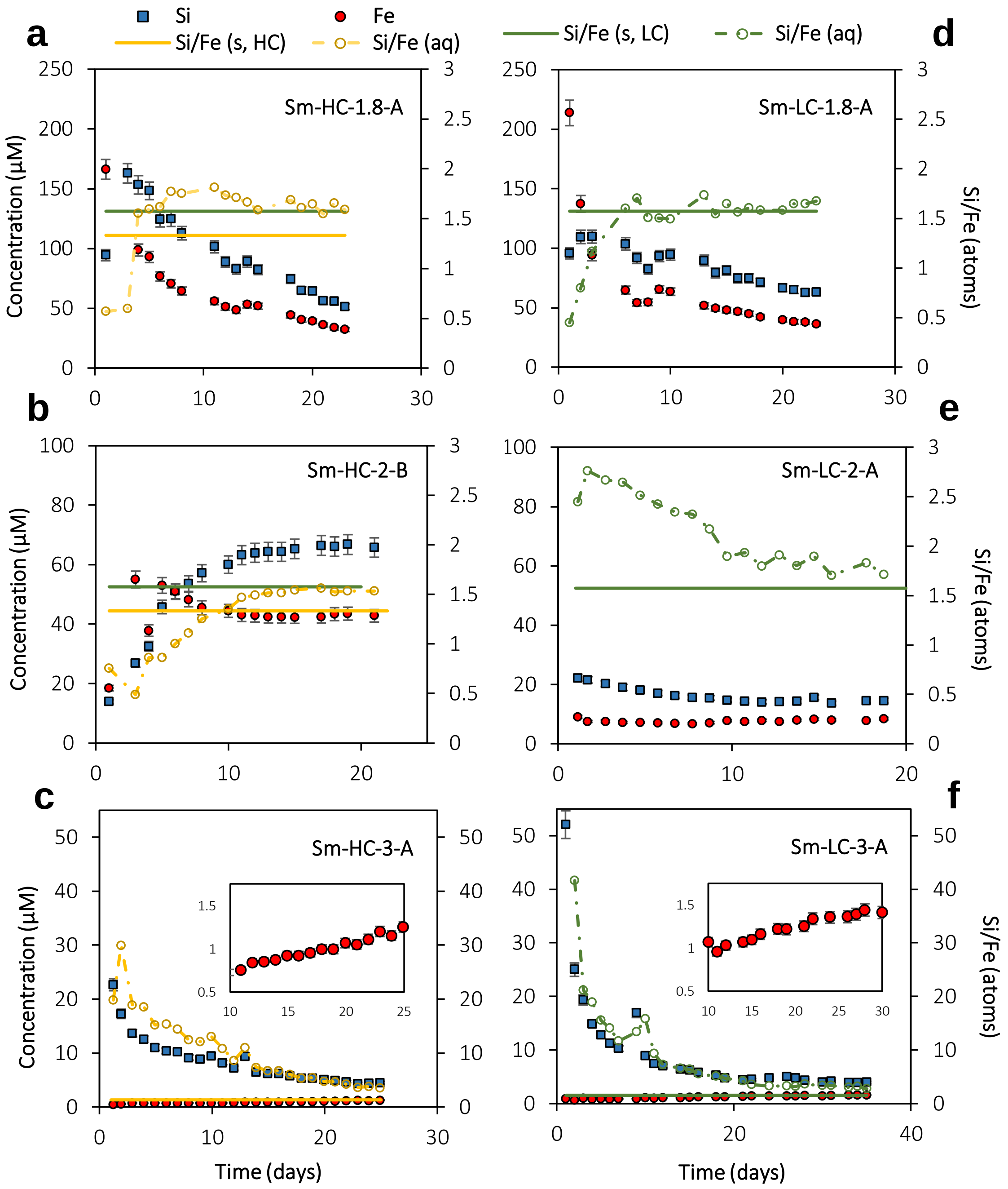

Fig. 2. Variation in the Si (blue square), Fe (red circle) and Mg (gray triangle) concentrations and the Si/Fe atomic ratio as a function of time in the output solutions (connected circles) of selected dissolution experiments. The first two characters in the names of the experiments denote the smectite crystal chemistry used, the next digit in the name is the pH, and the last letter indicates the type of reactor used. The solid Si/Fe ratio of the synthetic Fe(III)-rich smectites is represented by a

horizontal line. The concentrations of aqueous Fe in the experiments performed at pH 4 and 5 were below the quantification limit.

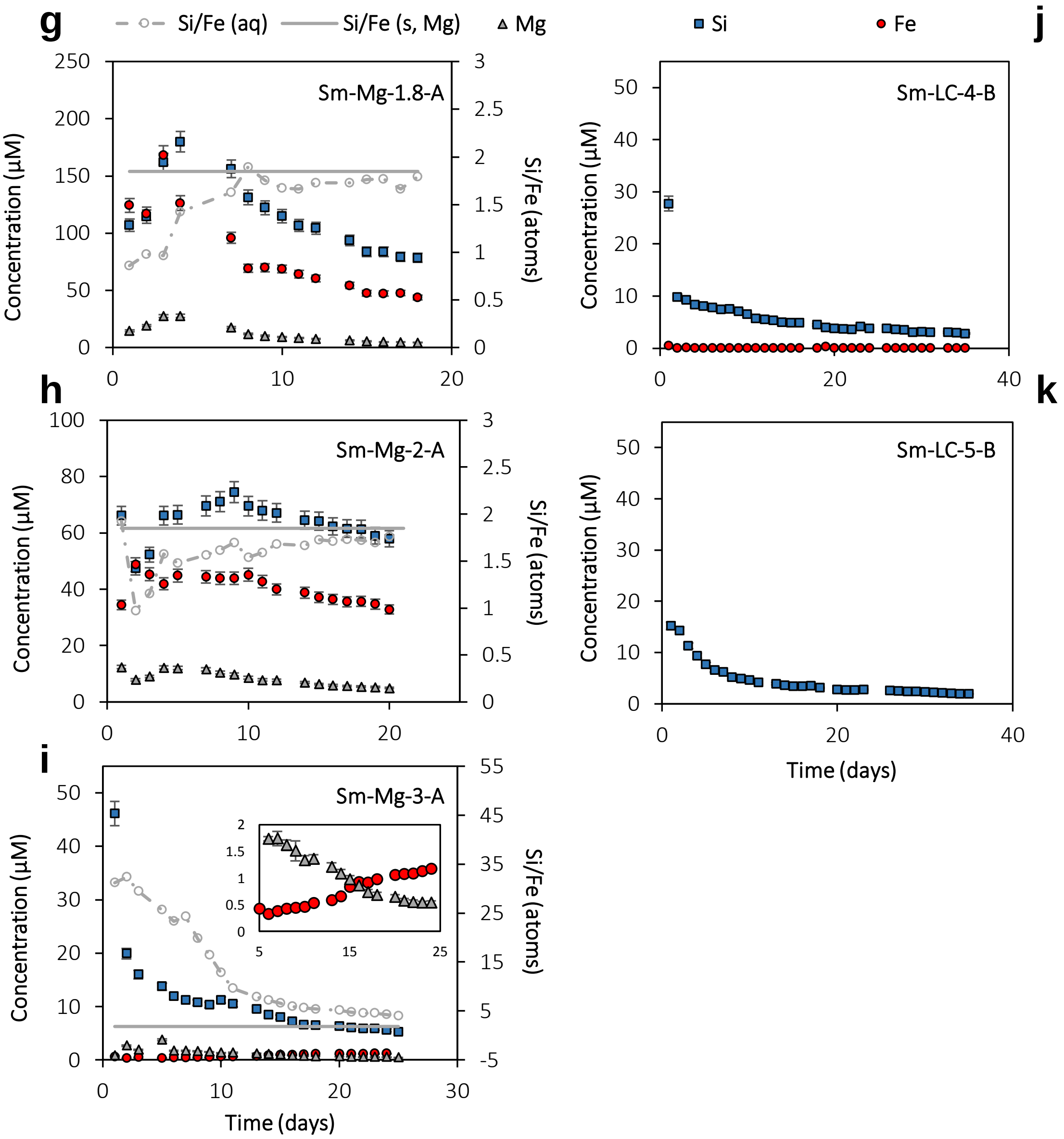

Fig. 2. (continued)

For the dissolution experiments performed at pH 1.8 and 2, all output Si concentrations (except for those in the Sm-HC-2-B experiment; Fig. 2b) increased during the first days of the experiment (between two and nine days) (Fig. 2 a, d, e, g and h). Afterward, the aqueous Si concentration decreased until it reached a steady state (between 12 and 15 days at pH 1.8 and between 10 and 12 days at pH 2). This evolution was not observed for experiments at pH≥3, which instead showed a continuous decrease in the output Si concentration from the beginning of the experiments until a steady state was reached (Fig. 2 c, f, i, j and k). For the experiments performed at pH 1.8 and 2 (except Sm-HC-2-B), the release of Fe in solution exhibited a trend similar to that of Si. At the beginning of the experiments performed at pH 3, the amount of Fe released was less than 0.6 µM but increased slowly with time. At steady state, the aqueous Fe concentration was twice the concentration measured in the first days (see insets in Figs. 2 c, f, i). For experiments performed at pH≥4, the Fe concentrations were below the quantification limit (<0.03 µM). For the experiments performed with Sm-Mg, the aqueous Mg concentration exhibited the same trend as that for the experiments carried out at pH≤3, with an increase in concentration in solution for six days, followed by a progressive decrease. The Mg release remained at a value of half of the Fe release, consistent with the low Mg content in the smectite structure (see Table 1). The average Si, Fe and Mg aqueous concentrations measured at the steady state in all the experiments are presented in Table S1. The output concentrations approached a steady state between 10 and 30 days depending on the dissolution conditions and/or crystal chemistries of the starting smectite. The time to reach the steady state was the longest for the Sm-LC sample under all pH conditions.

For the output solutions, different changes in the Si/Fe ratios were observed depending on the sample and the pH of the input solution. For the dissolution of Sm-LC at pH 1.8 (Fig. 2 d) and the dissolution of Sm-Mg at pH 1.8 and 2 (Fig. 2 g, h), the evolution of the Si/Fe ratios was divided into two steps. First, the Si/Fe ratios increased for 10 days, remaining lower than the solid stoichiometry values. Second, constant Si/Fe ratios close to the solid stoichiometry ratios were observed. The same trend was observed in the Sm-HC experiments, in which the first step lasted 12 days; however, during the second step, the constant Si/Fe ratios were not close to the Sm-HC solid stoichiometry but were instead close to the Sm-LC solid stoichiometry (see Fig. 2 a, b). Two steps were also observed in the Sm-LC experiment at pH 2 (Fig. 2 e); however, in that case, the Si/Fe ratio decreased toward the solid stoichiometry but remained slightly greater (9%). The same trend was observed at pH 3 for the three smectite samples, but the time to reach a constant Si/Fe value was longer (more than 16 days), and the solid stoichiometry was never reached during the experiment (maximum of 35 days).

For each steady state obtained experimentally, the saturation indexes of the output solutions were calculated with respect to the amorphous silica, Fe-bearing (ferrihydrite), and Mg-bearing (brucite) phases using the measured aqueous chemical composition (Table S1). The results were plotted against the output pH in the supplementary material file (Fig. S4 a, b, c). Saturation indexes for amorphous silica were reported as a function of time for experiments performed at pH 1.8 and pH 2 (Fig. S4 d). For all the experiments, the output solutions were undersaturated with respect to the amorphous silica, Fe-bearing, and Mg-bearing phases and Fe-rich smectites.

3.2. Solid analysis

The FTIR spectra of the initial Sm-HC and acidified Sm-HC samples retrieved at the end of the experiments are shown in Fig. 3. The spectra of Sm-LC and Sm-Mg are not shown, but the band positions of interest are listed in Table S2 (supplementary material). The spectra of the three crystal chemistries displayed an intense band in the Si-O stretching (ν) region (997 to 1015 cm^{-1}) at different positions depending on the crystal chemistry and pH (Fig. 3 a, Table S2). In the spectra on the initial Fe(III)-rich smectites, νSi-O vibrations were observed at 997, 1005, and 1006 cm^{-1} for Sm-HC (tetrahedral charge = 1.14), Sm-Mg (tetrahedral charge = 0.84) and Sm-LC (tetrahedral charge = 0.66), respectively. Overall, for the dissolved samples, the position of the νSi-O band shifted toward higher wavenumbers from the initial positions as the pH decreased (see Fig. 3 a, Table S2). The spectrum of the Sm-HC samples showed the greatest continuous shift, from 997 to 1010 cm^{-1} (Fig. 3 a), while that of Sm-Mg displayed a shift from 1005 to 1015 cm^{-1}. The spectra of these two samples displaed shifts at pH 5, whereas the spectra of the Sm-LC samples exhibited a significant shift from 1006 to 1012 cm^{-1} only at pH 1.8 (Table S2). The spectra showed a shoulder at approximately 1100 cm^{-1} for Sm-HC-1.8 and Sm-Mg-1.8 with similar intensities (Table S2, Fig. 3 a), but this feature was not present in the Sm-LC-1.8 spectrum. The Sm-HC (altered or not) spectra exhibited a band at 707 cm^{-1} (Fig. 3 b), which was attributed in part to tetrahedral $^{[4]}$Fe(III)-O vibrations (Decarreau et al., 2008). The intensity of the $^{[4]}$Fe(III)-O band increased as the tetrahedral Fe(III) content of the smectite samples increased (Fig. 4, Table S2). For the Sm-HC samples dissolved at acidic pH, the $^{[4]}$Fe(III)-O band continuously decreased in intensity as the pH decreased (Fig. 3 b).

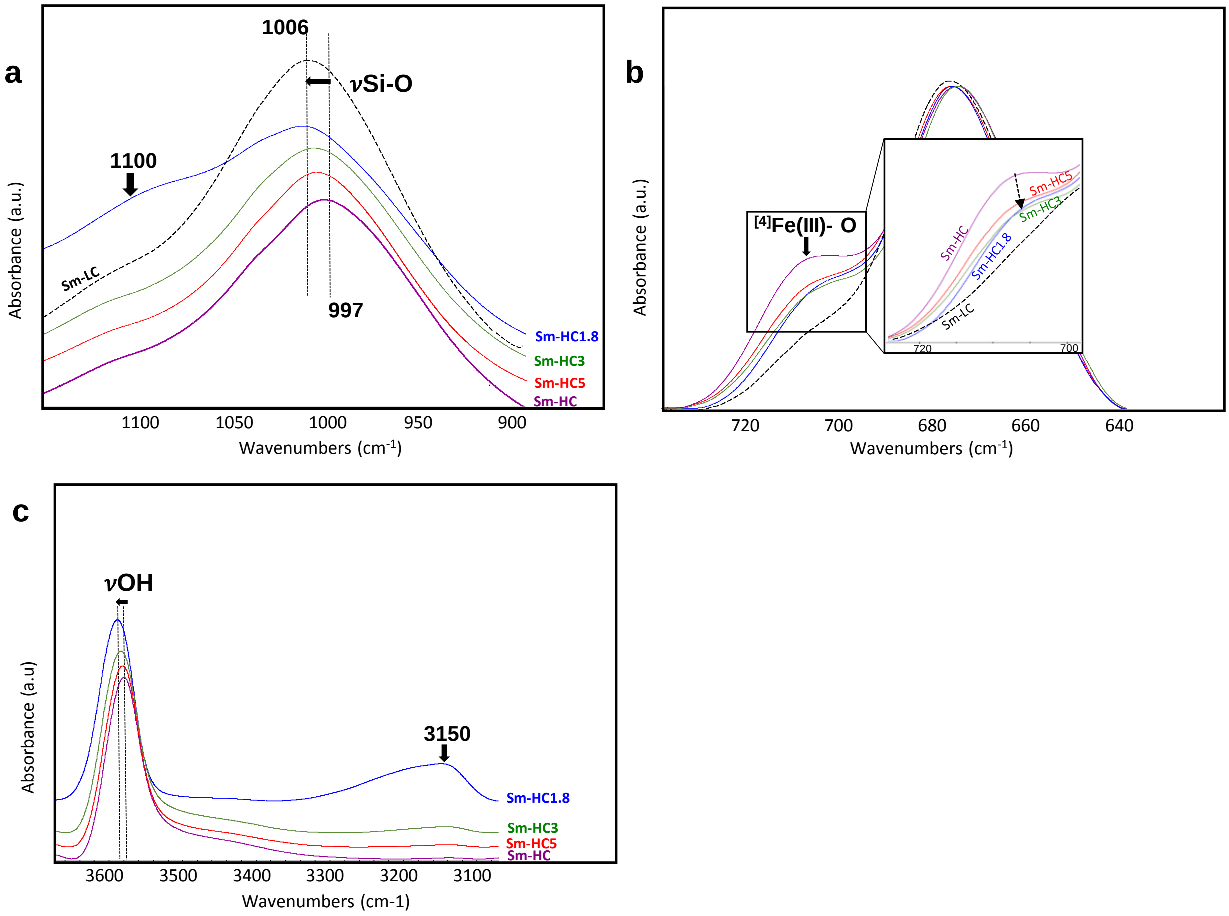

Fig. 3. MIR spectra of initial and altered Sm-HC samples at pH 1.8, 3, and 5 in the vSi-O region (a), in the $^{[4]}$Fe(III)-O vibration region (b) and in the vOH region (c). The black arrows indicate the shoulders and the shifts associated with the main modifications upon alteration. To help interpret the changes in the spectra of the Sm-HC sample upon alteration, the initial spectrum of the Sm-LC sample is also shown. For clarity, only the results of Sm-HC alteration experiments are shown here, and the data for Sm-LC and Sm-Mg alteration are reported in Table S2 in the supplementary material file.

The spectra of the initial Fe(III)-rich smectites exhibited an absorption band in the vOH region at 3559 cm^{-1} for Sm-HC and Sm-LC and at 3555 cm^{-1} for Sm-Mg (Table S2), which was attributed to νFe(III)$_2$OH. The small difference among samples was due to the presence of Mg atoms in the octahedral sheet. In the spectra of all the altered samples, the position of this band shifted toward higher wavenumbers (Fig. 3c), and the shifts were similar among the three samples (≈ 8 cm^{-1} between the initial and dissolved smectite phases at pH 1.8).

In the spectra of the three samples, a shoulder progressively appeared at 3150 cm^{-1} (identified by the black arrow in Fig. 3c). The intensity of this shoulder increased continuously as the pH decreased, with greater intensity for the samples dissolved at pH 1.8 and 2 (Table S2).

TEM observations of the Sm-LC initial particles and the Sm-LC samples dissolved at pH 3 and 1.8 revealed the morphological evolution of the particles (Fig. S5). The initial particles presented a lath shape that evolved after the dissolution experiments to form a rounded shape, accompanied by a decrease in the particle size (Fig. S5). HRTEM images of the altered Sm-HC particles at pH 3 showed alterations in the basal surface (Fig. S6b). A higher magnification image of Sm-HC-3 (Fig. S6d) showed a decrease in the crystallinity of some parts of the basal surface relative to the initial particles (Fig. S6a, c). No discrete Si-rich or amorphous phases were observed at the scale of the observation; however, their presence could not be completely excluded.

3.3. Fe(III)-rich smectite dissolution rates

The steady-state dissolution rates of Fe(III)-rich smectites are plotted as a function of pH in Fig. 4. The dissolution rates decreased with increasing pH. The dissolution rates for Sm-LC were lower than those for the Sm-HC samples, regardless of the pH. Note that greater differences between dissolution rates were observed at pH 1.8 and 2. The dissolution rates of the Sm-Mg samples were between those obtained for the two other smectites.

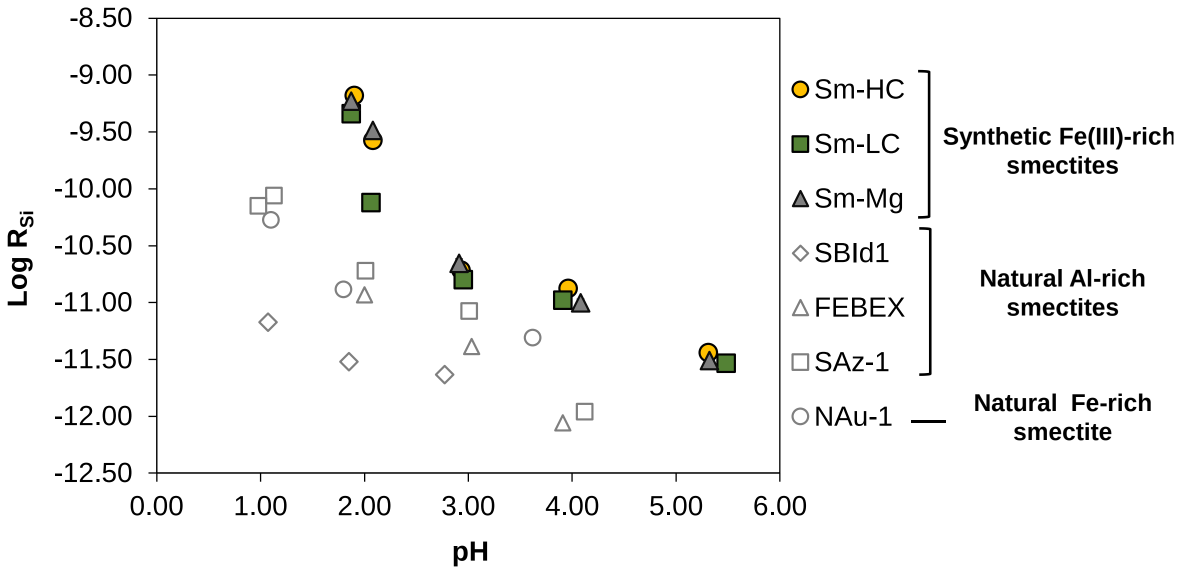

Fig. 4. Dissolution rates of Sm-HC, Sm-LC and Sm-Mg calculated in this study using equation (1) compared to the dissolution rates of natural SBId1, FEBAX, SAz-1, and NAu-1 from Robin et al. (2016), Cappelli et al. (2018), Amram and Ganor (2005) and Gainey et al. (2014), respectively.

The variations in the dissolution rates of Sm-HC, Sm-LC and Sm-Mg are plotted as a function of Gibbs free energy (Δ_rG) in Fig. 4a. In the Sm-LC experiments performed between pH 2.06 and 5.5, the calculated values of Δ_rG deviated from equilibrium as the rates increased. However, for the highest dissolution rate measured at pH 1.87 (R_{Si} = 4.47.10^{-10} g mol^{-1} s^{-1}), the associated Δ_rG value was closer to equilibrium (-5.24 kcal mol^{-1}) than the Δ_rG value calculated for Sm-LC at pH 4. This deviation of the Δ_rG values toward equilibrium was also observed for the experiments performed with Sm-HC and Sm-Mg. However, for these samples, the deviation was observed for two dissolution rates, namely, those measured at pH 2.08 and pH 1.90 for Sm-HC and those measured at pH 2.08 and 1.87 for Sm-Mg samples, for which the Δ_rG values were closer to equilibrium than those measured in the experiments carried out with Sm-HC and Sm-Mg at pH 4 (Fig. 4a).

4. Discussion

4.1. Effect of the crystal chemistry of synthetic Fe(III)-rich smectites on the dissolution rate

The variation in log R_{Si} as a function of pH for the three synthetic Fe(III)-rich smectites followed the same trend (Fig. 4). The rates decreased from pH 1.8 to 5.5, as observed for silicate dissolution rates at acidic pH (Marty et al., 2015). Similar log R_{Si} values were calculated (Fig. 4), even though Sm-LC tended to have lower dissolution rates than Sm-HC and Sm-Mg. In particular at pH 2, the dissolution rate of Sm-LC was three times lower than the dissolution rates of Sm-HC and Sm-Mg (Table S1). The common representation of dissolution rates on a log scale as a function of pH did not highlight important differences between the chemical reactivity of the three Fe(III)-rich smectites.

4.2. Evolution of the crystal chemistry during dissolution.

The steady-state aqueous Si/Fe ratios of Sm-HC at pH 1.8 and 2 were higher than the stoichiometric ratio of the starting material, while the Si/Fe aqueous ratio was stoichiometric for Sm-LC and Sm-Mg, characterized by a lower Fe(III) content (Fig. 2). This finding demonstrated the instability of Fe(III)-rich smectite with a high tetrahedral charge and high iron content and the preferential loss of Fe during dissolution (nonstoichiometric dissolution). FTIR analyses of the Sm-HC and Sm-Mg samples also revealed a significant decrease in the $^{[4]}$Fe(III) content with respect to the total Fe content under all pH conditions, as determined from the continuous shift in the νSi-O band in the spectra of the Sm-Mg samples and the continuous shift in the νSi-O band in conjunction with a decrease in the intensity of the $^{[4]}$Fe(III)-O band in the spectra of the Sm-HC samples (Baron et al., 2016) (Table S2). In contrast, for the Sm-LC samples, the shift in the νSi-O vibration was significant only for the experiment at pH 1.8, and a decrease in the intensity of the $^{[4]}$Fe(III)-O vibration was not observed (Table S2). These results indicated that Sm-HC and, to a lesser extent, Sm-Mg were subject to changes in crystal chemistry during dissolution at acidic pH. A higher reactivity of the Sm-HC sample was also determined from the TEM images, which showed partial disorganization of the crystal structure after acidic dissolution at pH 3 (Fig. S6b and d). The decrease in the crystalline order was not homogeneous over the basal surface but was localized (Fig. S6d). Specifically, 5 nm spots with low structural order covered all the particles (white spots in Fig. S6b) and were attributed to reorganization of the crystal structure in response to the loss of tetrahedral Fe(III), as observed via aqueous and FTIR measurements. This uncommon feature of smectites was attributed to the high amount of tetrahedral Fe(III) substitutions for Si(IV), which caused a large distortion of the tetrahedral layer and consequently a high local energy environment that favored dissolution on the basal surface of the smectites. Cappelli et al. (2020) observed the formation of etch-pits during biotite dissolution at pH 1-2, in the presence of oxalic acid (at 0.01 M and 0.1 M) and at temperature between 25°C and 70°C. The alteration of biotite occurred far from equilibrium (-138 kcal mol^{-1} $< \Delta_r G < -131$ kcal mol^{-1}). In the present study, dissolution features comparable to those observed by Cappelli et al. (2020) were observed after the dissolution of the synthetic Fe(III)-rich smectites under less drastic conditions (HNO_3 0.001 M, 25°C) and closer to equilibrium conditions (-10 kcal mol^{-1} $< \Delta_r G < -1$ kcal mol^{-1}) (Fig. 5a), revealing the high reactivity of these minerals.

4.3. The role of aqueous Fe and Si on the Fe(III)-rich smectite dissolution

Regarding the fate of Fe during dissolution, no Fe-rich phase was detected. The output solutions were continuously undersaturated with respect to Fe-hydroxide over the full pH range investigated (Fig. S4). However, the Si/Fe aqueous ratios measured at steady state were at least two times greater than the Si/Fe ratios of the starting materials (Fig. 2) for all the experiments performed at pH 3 (Sm-HC-3, Sm-LC-3, Sm-Mg-3). For all the experiments performed at pH 4 and pH 5, the Fe concentrations were below the detection limits, regardless of the crystal chemistry of the smectite, which indicated an Fe deficit during the dissolution experiments (Fig. 2, Fig. S3). Several authors have attributed the Al or Fe deficit in solution to the adsorption of dissolved metals on cation exchanger sites during smectite dissolution experiments (Golubev et al., 2006; Rozalén et al., 2008; Gainey et al., 2014; Robin et al., 2016).

An initial increase in the Si aqueous concentration has been observed for natural smectites (Metz et al., 2005; Amram and Ganor 2005; Gainey et al., 2014) and other clay minerals (Cama et al., 2002; Viennet et al., 2016; Smith et al., 2017). The rapid release of Si in the first days of the experiment may have been caused by the dissolution of ultrafine amorphous silica particles, which dissolve faster than smectite under acidic conditions (Metz et al., 2005; Amram and Ganor, 2005). In the present study, even though the presence of amorphous silica particles in the initial smectite samples could not be excluded, amorphous silica particles were not detected in the initial samples by FTIR or TEM (Fig. S1, Fig. S5). It is likely that the release of Si was caused by the dissolution of smaller smectite particles, considering the similar release of Si and Fe during the first days of the experiments (Fig. 2). However, during these initial days, the dissolution was not stoichiometric at pH 1.8 or 2. A deficit of Si with respect to Fe was observed (except for in Sm-LC-2), as was the case for Fe and/or Al during dissolution experiments performed with natural smectites (Cama et al., 2000; Rozalén et al., 2008; Robin et al., 2016). In our study, no distinct Si-rich particles were observed by TEM after dissolution, and all the output solutions were undersaturated with respect to amorphous silica (Fig. S4). However, the FTIR spectra of the Sm-HC-1.8 and Sm-Mg-1.8 samples displayed a shoulder at 1100 cm^{-1} on the large νSi-O bands and a continuous increase in the intensity of the band at 3150 cm^{-1} as the pH decreased. These two bands were observed during the dissolution experiments of smectites under acidic conditions and were attributed to the presence of a hydrated amorphous silica layer (Komadel, 1996; Madejová et al., 2009; Robin et al., 2016). Therefore, despite undersaturation with respect to amorphous silica, these results indicated the potential formation of an amorphous Si-rich phase in the samples with the highest total layer charge at acidic pH (pH < 3) (Table S2). While precipitation of amorphous silica has commonly been observed during the dissolution of smectites at pH ≤ 1 and 35°C (Komadel, 1996; Barrios et al., 2001; Shaw and Jim Hendry, 2009; Madejová et al., 2009), the present study demonstrates the potential formation of a Si-rich layer under less acidic conditions (1.8 ≤ pH ≤ 3). Previous studies have shown that the formation of an amorphous layer on the surface of smectite particles results in a coating that affects the release of elements (Turpault and Trotignon, 1994; Metz et al., 2005; Kameda et al., 2009; Schott et al., 2012). Even if such a layer did not form in our experiments, as demonstrated by the stoichiometric ratios at steady state, the potential formation of a Si-rich layer at acidic pH is important for achieving a better understanding of the alteration of smectites under natural conditions.

4.4. Effects of crystal chemistry on smectite reactivity: insights from comparisons with natural smectites from the literature

The dissolution rates (R_{Si}) of the three Fe(III)-rich synthetic smectites at different pH values were comparable to those of natural dioctahedral smectites (particle size ≤ 200 nm, similar to the synthetic smectites used in this study) containing Al and Fe (Fig. 4). The natural smectites were two montmorillonites (SAz-1 and FEBEX; Amram and Ganor 2005, Cappelli et al., 2018), a beidellite (SBId1; Robin et al., 2016) and a nontronite (NAu-1; Gainey et al., 2014). These studies were selected because of the variety of smectite crystal chemical properties included and because the experimental procedures used were similar to those used in the current study . Details of their respective structural formulas are available in the supplementary material (Table S3).

Dissolution rates of Fe(III)-rich smectites. The nontronite NAu-1 contains a slightly lower content of total Fe than the synthetic samples presented here (Table S3, Table 1). It has a total charge (1.06) similar to that of Sm-HC (1.14) and a predominant tetrahedral charge (96%) similar to those of Sm-HC and Sm-LC (Table 1). Despite these similarities, the dissolution rates of NAu-1 were reported to be 2 to 35 times lower than those of Sm-LC and between 3 and 50 times lower than those of Sm-HC (Fig. 4). Furthermore, the Sm-Mg synthetic smectite was found to have a different layer charge distribution than that of NAu-1. Similary, the dissolution rate of synthetic smectite was greater (2 to 44 times) than that of natural smectite (Fig. 4). For Fe(III)-rich smectites, neither the location nor the amount of total charge could explain the significant difference in dissolution rates. However, in NAu-1, the tetrahedral charge was caused by the substitutions of Al(III) for Si(IV) and a small amount of Al(III) was in the octahedral sheets, while no Al(III) was present in the synthetic samples. The total amount of structural Fe and/or the nature of the tetrahedral substitution (Al or Fe) had a significant impact on the dissolution rate of Fe(III)-rich smectites.

Comparison between Fe(III)-rich and Al-rich smectites. FEBEX and SAz-1, two montmorillonites, exhibited similar dissolution rates (Fig. 4) despite a significant difference in total charge (SAz-1 has a total charge 1.8 times greater than that of FEBEX; Table S3). However, their dissolution rates at pH 2 were 4 times greater than those of SBId1 beidellite (Fig. 4), whose total charge was between those of the two montmorillonites (Table S3). The natural Fe(III)-rich smectite (NAu-1) displayed higher dissolution rates than SBId1 beidellite (8 to 4 times higher at pH 1.1 and pH 2, respectively) despite a similar total charge, which was mainly attributed to tetrahedral substitutions, but the observed rate was within the range of rates exhibited by other Al-rich smectites with varying amounts of octahedral charge. The synthetic Fe(III)-rich smectites exhibited systematically higher dissolution rates than the Al-rich smectites, regardless of the charge location or total charge value (Fig. 5 Fig. 4). Thus, neither the total structural charge nor its location could explain the different reactivities of the smectites. This study highlights the effect of the structural Fe(III) content on mineral reactivity (i.e., the amount of Fe(III) in the octahedral sheets was 16 times greater in NAu-1 than in SBId1). A low content of structural Fe(III) combined with the stabilizing effect of tetrahedral Al(III) led to the strong stability of the Al-rich smectites. This is consistent with the behaviors of NAu-1 and FEBEX, which have similar dissolution rates but different crystal chemistries (more Fe(III) and more tetrahedral Al in NAu-1 versus less tetrahedral Al and more octahedral Mg in FEBEX). These results confirmed the stabilizing effect of Al described by Novák and Čížel (1978), Gainey et al. (2014) and Robin et al. (2016). These authors suggested that the substitutions could be considered as localized defects, that cause deformation and/or weakening of the structure, which impacts the reactivity of the particles, with different effects depending on the substituted ion. Additionally, Gainey et al. (2014) suggested that Al-rich and Fe(III)-rich smectites may have different behaviors as a result of surface protonation, which may also lead to different dissolution rates. The increasing reactivity of smectites as the Fe content increases could account for the systematically higher dissolution rates and strong instability of synthetic Fe(III)-rich smectites. The synthetic Fe(III)-rich smectites contained between 33% and 43% structural Fe(III) and no structural Al, which could result in stabilization (tetrahedral charges were caused by only Fe(III) substitutions for Si(IV)). Note that other substitutions, with Mg, seemed to affect the smectite reactivity. Indeed, our results showed that with a relatively similar amount of tetrahedral iron, Sm-Mg showed greater crystal chemical evolution than Sm-LC (Table S2). In addition, among the natural Al-rich smectites, it was the smectite richest in Mg (SAz-1) which reacted the fastest (Fig. 4).

5. Smectite dissolution rates laws

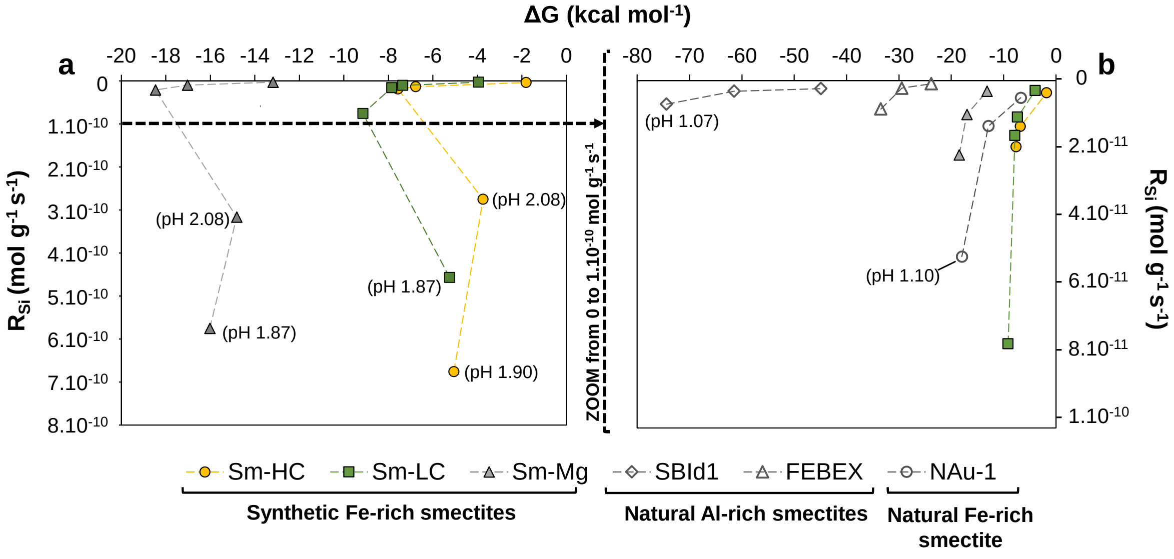

Fig. 5: Variation in dissolution rates (R_{Si} normalized to the mass) as a function of Gibbs free energy (Δ_rG) for (a) Sm-HC, Sm-LC and Sm-Mg at pH 1.8-5.5 (the pHs for which abnormal behaviors were observed are highlighted) and (b) Sm-HC and Sm-Mg at pH 3-5.5 and Sm-LC at pH 2-5.5 (zoom of Fig. 5a) and for three natural smectites, i.e., SBId1, FEBEX, and NAu-1, for which the values were calculated from the studies of Robin et al. (2016), Cappelli et al. (2018) and Gainey et al. (2014), respectively (see details in the supplementary material file, Table S4).

The variation in dissolution rates as a function of Gibbs free energy was similar between the three synthetic Fe(III)-rich smectites (Fig. 5a). Between pH 3 and 5.5, the dissolution rates increased as the system shifted further from equilibrium, with a nonlinear change in R_{Si} as a function of Δ_rG, as for other natural minerals (Fig. 5a, b). Then, at pH 1.8 and 2 for Sm-HC and Sm-Mg, and only at pH 1.87 for Sm-LC, the R_{Si} increased as the Δ_rG shifted toward equilibrium (Fig. 5a). Thus, for these samples, the relation between R_{Si} and Δ_rG did not follow the positive correlation between the dissolution rate and the distance from equilibrium expected for such a system. These deviations from the expected behavior of a silicate mineral observed at more acidic pH occurred because of important structural changes (decrease in permanent charge) and the formation of an amorphous silica phase (see discussion section 3.2, Fig. 3, and Table S2). A significant change in the solid during the reaction could explain the difficulty to compute a consistent Δ_rG.

Only the dissolution rates of Sm-HC and Sm-Mg at pH 3–5.5 and those of Sm-LC at pH 2–5.5 (the samples with the lowest changes in crystal chemistry) are shown in Fig. 5b, as are those of beidellite, nontronite and Al-rich montmorillonite for further comparison. A different behavior was observed between the Fe(III)-rich and Al-rich smectites; i.e., the Fe(III)-rich smectites exhibited the highest dissolution closer to equilibrium. This highlights the greater reactivity of Fe(III)-rich smectites than of Al-rich smectites. The expected evolution of the $R_{Si}=f(\Delta_rG)$ function at pH 1.1 for Nau-1, i.e., a continuous increase in dissolution rate as a function of decreasing Δ_rG, demonstrates the important role of Al substitutions in the tetrahedral sheets, allowing structural stabilization, and confirms that the high instability of Fe(III)-rich smectites is mainly due to Fe(III) substitutions for Si(IV) in clay sheets. The destabilizing effect of the substitutions by Mg in the octahedral sheets was confirmed by the change in behavior observed for Sm-Mg from pH 2.08 (Fig 5a). Nevertheless, additional experimental data are needed to quantify the exact effect of the presence of structural Mg compared with that of structural Fe. Thus, Fe(III)-rich smectites do not systematically satisfy the conditions for proposing a general dissolution rate law allowing us to extrapolate their behavior because of the evolution of their crystal chemistry during dissolution.

Cappelli et al. (2018) proposed a dissolution rate law for an Al-rich montmorillonite used in an engineered clay barrier. However, according to our results, a different dissolution rate law is required for Fe(III)-rich smectites, which may be present in many environments, particularly in soils.

5. Conclusion and Perspectives

The effects of the crystal chemistry and pH on the dissolution rates of Fe(III)-rich smectites with small particle sizes (<100 nm) were studied at pH values between 1.8 and 5.5 and at room temperature. The permanent charge and the amount of Fe in the structure were the main parameters affecting the reactivity of Fe(III)-rich smectites. An initial high total charge (>0.6 by $O_{20}(OH)_4$) resulted in the instability of smectites in solution, with mineral evolution characterized by a loss of tetrahedral charge and the potential formation of a Si-rich layer. When the pH decreased, the Fe(III)-rich smectites formed a common lower charge structure. Additionally, natural Al-bearing smectites were found to exhibit greater stability than Fe-rich smectites under conditions far from equilibrium. These results indicated the significant effect of the crystal chemistry of the smectites on their dissolution (dissolution rate, dissolution stoichiometry) under acidic conditions.

Thus, the use of a single rate law to describe the dissolution rate of smectites must be considered with caution. It is important to consider the crystal chemistry of smectites, i.e., the amount and nature of the isomorphic substitutions, to account for the reactivity of these clays. This study showed that the use of a rate law may be limited to acidic pH. Therefore, it might be interesting to complete these observations with other synthetic samples with greater heterogeneity between the nature, location, and amount of isomorphic substitutions to assess the sensitivity of the effects of the crystal chemistry on the variability between rate laws. However, particular attention must be given to the transformations that can occur on solids (crystal-chemical changes, precipitation) even at moderate pH and temperature before predicting the evolution of minerals. Conclusions put forward by Kohler et al. (2004) reinforce this conclusion, indicating that the steady state condition needs to be clearly defined during the experimental approach because clay mineral dissolution may not attain a “true” steady state due to the morphological modifications of solids over time, i.e., the relative increase in the average basal surface compared to edge surfaces. In any case, this study clearly shows the rapid evolution of Fe(III)-rich clay minerals in the environment even for slight physicochemical variations, which is a critical issue at a larger scale toward global changes through the evolution of the availability of nutrients and other elements in soils and surface environments.

Acknowledgments

Part of this research was funded by Region Nouvelle-Aquitaine, France (“MobiMet” project, AAP ESR 2020), and the CNRS-EC2CO program (project “ALMA”).

Data Availability

Data are available through Mendeley Data at https://data.mendeley.com/datasets/r7sz6d2sww/1.

Appendix A. Supplementary material

The Supplementary Materials contains Supplementary Figure 1 and Supplementary Figure 2, providing infrared spectra and X-ray diffraction patterns of unaltered synthetic samples, respectively; Supplementary Table 1, indicating the experimental conditions and the results of the experiments; Supplementary Figure 3, showing the evolution of the concentrations of aqueous Si, Fe, and Mg measured as a function of time in the output solutions during dissolution experiments performed at pH 4 and 5.5 with Sm-HC and Sm-Mg; Supplementary Figure 4, illustrating the saturation indexes of the output solutions with respect to amorphous silica and Fe- and Mg- bearing phases and each synthetic smectite; Supplementary Table 2, indicating the FTIR spectra of dissolved Fe(III)-rich smectites; Supplementary Figures 5 and 6, showing the TEM and HRTEM observations of unaltered and altered Fe(III)-rich smectites; Supplementary Table 3, indicating the crystal chemical properties of the natural smectites mentioned in this study; and Supplementary Table 4, providing data related to the dissolution of SBId1 and Nau-1, which were obtained from the literature and used to calculate the Gibbs free energies (shown in Figure 6).

References

Amram, K., Ganor, J., 2005. The combined effect of pH and temperature on smectite dissolution rate under acidic conditions. Geochim. Cosmochim. Acta 69, 2535–2546.

Badraoui, M., Bloom, P.R., 1990. Iron-Rich High-Charge Beidellite in Vertisols and Mollisols of the High Chaouia Region of Morocco. Soil Sci. Soc. Am. J. 54, 267–274.

Bakker, E., Hubert, F., Wander, M.M., Lanson, B., 2018. Soil Development under Continuous Agriculture at the Morrow Plots Experimental Fields from X-ray Diffraction Profile Modelling. Soil Systems 2, 46.

Bakker, E., Lanson, B., Findling, N., Wander, M.M., Hubert, F., 2019. Mineralogical differences in a temperate cultivated soil arising from different agronomic processes and plant K-uptake. Geoderma 347, 210–219.

Baron, F., Petit, S., Tertre, E., Decarreau, A., 2016. Influence of Aqueous Si and Fe Speciation on Tetrahedral Fe(III) Substitutions in Nontronites: a Clay Synthesis Approach. Clays Clay Miner. 64, 230–244.

Barrios, M.S., de Santiago Buey, C., Romero, E.G., Pozas, J.M.M., 2001. Textural and structural modifications of saponite from Cerro del Aguila by acid treatment. Clay Miner. 36, 483–488.

Bibi, I., Singh, B., Silvester, E., 2011. Dissolution of illite in saline–acidic solutions at 25°C. Geochim. Cosmochim. Acta 75, 3237–3249.

Blanc, P., Gherardi, F., Vieillard, P., Marty, N.C.M., Gailhanou, H., Gaboreau, S., Letat, B., Geloni, C., Gaucher, E.C., Madé, B., 2021. Thermodynamics for clay minerals: Calculation tools and application to the case of illite/smectite interstratified minerals. Appl. Geochem. 130, 104986.

Blanc, P., Lassin, A., Piantone, P., Azaroual, M., Jacquemet, N., Fabbri, A., Gaucher, E.C., 2012. Thermoddem: A geochemical database focused on low temperature water/rock interactions and waste materials. Appl. Geochem. 27, 2107–2116.

Cama, J., Ganor, J., Ayora, C., Lasaga, C.A., 2000. Smectite dissolution kinetics at 80°C and pH 8.8. Geochim. Cosmochim. Acta 64, 2701–2717.

Cama, J., Metz, V., Ganor, J., 2002. The effect of pH and temperature on kaolinite dissolution rate under acidic conditions. Geochim. Cosmochim. Acta 66, 3913–3926.

Cappelli, C., Cama, J., Van Driessche, A.E.S., Huertas, F.J., 2020. Biotite reactivity in nitric and oxalic acid at low temperature and acid pH from surface and bulk dissolution measurements. Chem. Geol. 554, 119806.

Cappelli, C., Yokoyama, S., Cama, J., Huertas, F.J., 2018. Montmorillonite dissolution kinetics: Experimental and reactive transport modeling interpretation. Geochim. Cosmochim. Acta 227, 96–122.

Chorover, J., Amistadi, M.K., 2001. Reaction of forest floor organic matter at goethite, birnessite and smectite surfaces. Geochim. Cosmochim. Acta 65, 95–109.

Daval, D., Hellmann, R., Saldi, G.D., Wirth, R., Knauss, K.G., 2013. Linking nm-scale measurements of the anisotropy of silicate surface reactivity to macroscopic dissolution rate laws: New insights based on diopside. Geochim. Cosmochim. Acta 107, 121–134.

Ferret, C., Sterckeman, T., Cornu, J.-Y., Gangloff, S., Schalk, I.J., Geoffroy, V., 2014. Siderophore-promoted dissolution of smectite by fluorescent Pseudomonas. Environ. Microbiol. Rep. 6, 459–467.

França, D.B., Oliveira, L.S., Filho, F.G.N., Filho, E.C.S., Osajima, J.A., Jaber, M., Fonseca, M.G., 2022. The versatility of montmorillonite in water remediation using adsorption: Current studies and challenges in drug removal. Journal of Environmental Chemical Engineering 10, 107341.

Gainey, S.R., Hausrath, E.M., Hurowitz, J.A., Milliken, R.E., 2014. Nontronite dissolution rates and implications for Mars. Geochim. Cosmochim. Acta 126, 192–211.

Golubev, S.V., Bauer, A., Pokrovsky, O.S., 2006. Effect of pH and organic ligands on the kinetics of smectite dissolution at 25°C. Geochim. Cosmochim. Acta 70, 4436–4451.

Grybos, M., Michot, L.J., Skiba, M., Billard, P., Mustin, C., 2010. Dissolution of anisotropic colloidal mineral particles: Evidence for basal surface reactivity of nontronite. J. Colloid Interface Sci. 343, 433–438.

Haack, E.A., Johnston, C.T., Maurice, P.A., 2008. Mechanisms of siderophore sorption to smectite and siderophore-enhanced release of structural Fe3+. Geochim. Cosmochim. Acta 72, 3381–3397.

Hubert, F., Caner, L., Meunier, A., Ferrage, E., 2012. Unraveling complex <2 µm clay mineralogy from soils using X-ray diffraction profile modeling on particle-size sub-fractions: Implications for soil pedogenesis and reactivity. Am. Mineral. 97, 384–398.

Jalal, F.E., Xu, Y., Li, X., Jamhiri, B., Iqbal, M., 2021. Fractal approach in expansive clay-based materials with special focus on compacted GMZ bentonite in nuclear waste disposal: a systematic review. Environ. Sci. Pollut. Res. 28, 43287–43314.

Jayrajsinh, S., Shankar, G., Agrawal, Y.K., Bakre, L., 2017. Montmorillonite nanoclay as a multifaceted drug-delivery carrier: A review. Journal of Drug Delivery Science and Technology 39, 200–209.

Kameda, J., Sugimori, H., Murakami, T., 2009. Modification to the crystal structure of chlorite during early stages of its dissolution. Phys. Chem. Minerals. 36, 537–544.

Kaufhold, S., Dohrmann, R., Degtjarev, A., Koeniger, P., Post, V., 2019. Mg and silica release in short-term dissolution tests in bentonites. App. Clay Sci. 172, 106–114.

Köhler, S.J., Bosbach, D., Oelkers, E.H., 2005. Do clay mineral dissolution rates reach steady state? Geochim. Cosmochim. Acta 69, 1997–2006.

Komadel, P., 1996. Dissolution of Hectorite in Inorganic Acids. Clays Clay Miner. 44, 228–236.

Laird, D.A., Barak, P., Nater, E.A., Dowdy, R.H., 1991. Chemistry of Smectitic and Illitic Phases in Interstratified Soil Smectite. Soil Sci. Soc. Am. J. 55, 1499–1504.

Madejová, J., Pentrák, M., Pálková, H., Komadel, P., 2009. Near-infrared spectroscopy: A powerful tool in studies of acid-treated clay minerals. Vibrational Spectroscopy 49, 211–218.

Martin, L.A., Wissocq, A., Benedetti, M.F., Latrille, C., 2018. Thallium (Tl) sorption onto illite and smectite: Implications for Tl mobility in the environment. Geochim. Cosmochim. Acta 230, 1–16.

Marty, N.C.M., Cama, J., Sato, T., Chino, D., Villiéras, F., Razafitianamaharavo, A., Brendlé, J., Giffaut, E., Soler, J.M., Gaucher, E.C., Tournassat, C., 2011. Dissolution kinetics of synthetic Na-smectite. An integrated experimental approach. Geochim. Cosmochim. Acta 75, 5849–5864.

Marty, N.C.M., Claret, F., Lassin, A., Tremosa, J., Blanc, P., Madé, B., Giffaut, E., Cochepin, B., Tournassat, C., 2015. A database of dissolution and precipitation rates for clay-rocks minerals. Appl. Geochem. 55, 108–118.

Metz, V., Amram, K., Ganor, J., 2005. Stoichiometry of smectite dissolution reaction. Geochim. Cosmochim. Acta 69, 1755–1772.

Metz, V., Ganor, J., 2001. Stirring effect on kaolinite dissolution rate. Geochim. Cosmochim. Acta 65, 3475–3490.

N'Guessan, N.E., Joussein, E., Courtin-Nomade, A., Paineau, E., Soubrand, M., Grauby, O., Robin, V., Cristina, C.D., Vantelon, D., Launois, P., Fondanèche, P., Rossignol, S., Texier-Mandoki, N., Bourbon, X., 2021. Role of cations on the dissolution mechanism of kaolinite in high alkaline media. App. Clay Sci. 205, 106037.

Novák, I., Číčel, B., 1978. Dissolution of Smectites in Hydrochloric Acid: II. Dissolution Rate as a Function of Crystallochemical Composition. Clays Clay Miner. 26, 341–344.

Parkhurst, D.L., Appelo, C.A.J., 1999. User's guide to PHREEQC (Version 2): A computer program for speciation, batch-reaction, one-dimensional transport, and inverse geochemical calculations. Water-resources investigations report, 99(4259), 312.

Parrello, D., Zegeye, A., Mustin, C., Billard, P., 2016. Siderophore-Mediated Iron Dissolution from Nontronites Is Controlled by Mineral Cristallochemistry. Front. Microbiol. 7.

Ramos, M.E., Cappelli, C., Rozalén, M., Fiore, S., Huertas, F.J., 2011. Effect of lactate, glycine, and citrate on the kinetics of montmorillonite dissolution. Am. Mineral. 96, 768–780.

Ramos, M.E., Garcia-Palma, S., Rozalen, M., Johnston, C.T., Huertas, F.J., 2014. Kinetics of montmorillonite dissolution: An experimental study of the effect of oxalate. Chem. Geol. 363, 283–292.

Robin, V., Beaufort, D., Tertre, E., Reinholdt, M., Fromaget, M., Forestier, S., de Boissezon, H. Descostes, M., 2020. Fate of dioctahedral smectites in uranium roll front deposits exploited by acidic In Situ Recovery (ISR) solutions. App. Clay Sci. 187, 105484.

Robin, V., Tertre, E., Regnault, O., Descostes, M., 2016. Dissolution of beidellite in acidic solutions: Ion exchange reactions and effect of crystal chemistry on smectite reactivity. Geochim. Cosmochim. Acta 180, 97–108.

Rozalen, M., Huertas, F.J., Brady, P.V., 2009. Experimental study of the effect of pH and temperature on the kinetics of montmorillonite dissolution. Geochim. Cosmochim. Acta 73, 3752–3766.

Rozalén, M. L., Huertas, F.J., Brady, P.V., Cama, J., García-Palma, S., Linares, J., 2008. Experimental study of the effect of pH on the kinetics of montmorillonite dissolution at 25°C. Geochim. Cosmochim. Acta 72, 4224–4253.

Schott, J., Pokrovsky, O.S., Spalla, O., Devreux, F., Gloter, A., Mielczarski, J.A., 2012. Formation, growth and transformation of leached layers during silicate minerals dissolution: The example of wollastonite. Geochim. Cosmochim. Acta 98, 259–281.

Shaw, S.A., Jim Hendry, M., 2009. Geochemical and mineralogical impacts of H2SO4 on clays between pH 5.0 and −3.0. Appl. Geochem. 24, 333–345.

Smith, M.M., Dai, Z., Carroll, S.A., 2017. Illite dissolution kinetics from 100 to 280°C and pH 3 to 9. Geochim. Cosmochim. Acta 209, 9–23.

Strickland, J.D.H., Parsons, T.R., 1972. A Practical Handbook of Seawater Analysis. Fisheries Research Board of Canada, Ottawa.

Stucki, J.W., Goodman, B.A., Schwertmann, U., 1987. Iron in Soils and Clay Minerals., Springer Netherlands, Dordrecht.

Tessier, D., Pédro, G., 1985. Mineralogical Characterization of 2:1 Clays in SoilsImportance of the Clay Texture. In Proceedings of the International Clay Conference Denver, 1985 Clay Minerals Society.

Turpault, M.-P., Trotignon, L., 1994. The dissolution of biotite single crystals in dilute HNO3 at 24°C: Evidence of an anisotropic corrosion process of micas in acidic solutions. Geochim. Cosmochim. Acta 58, 2761–2775.

Viennet, J.-C., Hubert, F., Ferrage, E., Tertre, E., Legout, A., Turpault, M.-P., 2015. Investigation of clay mineralogy in a temperate acidic soil of a forest using X-ray diffraction profile modeling: Beyond the HIS and HIV description. Geoderma 241–242, 75–86.

Viennet, J.-C., Hubert, F., Tertre, E., Ferrage, E., Robin, V., Dzene, L., Cochet, C., Turpault, M.-P., 2016. Effect of particle size on the experimental dissolution and auto-aluminization processes of K-vermiculite. Geochim. Cosmochim. Acta 180, 164–176.

Vorhies, J.S., Gaines, R.R., 2009. Microbial dissolution of clay minerals as a source of iron and silica in marine sediments. Nat. Geosci. 2, 221–225.

Wells, D.E., Krakiwsky, E.J., 1971. The method of least sqaures (Vol.18).,

Wilson, M.J., 1999. The origin and formation of clay minerals in soils: past, present and future perspectives. Clay miner. 34, 7–25.

Role of the crystal chemistry on the dissolution kinetics of Fe(III)-rich smectites

D. Masson[1], V. Robin[1], E. Joussein[1], E. Tertre[2] & F. Baron[2]

[1]Université de Limoges, E2Lim UR 24133, 123 av. A. Thomas, 87060 Limoges Cedex, France

[2]Université de Poitiers, IC2MP UMR CNRS 7285, 4 rue M. Brunet, 86022 Poitiers Cedex, France

SUPPLEMENTARY MATERIAL

1. Additional description of initial Fe(III)-rich smectites

1.1. Infrared spectroscopy analysis

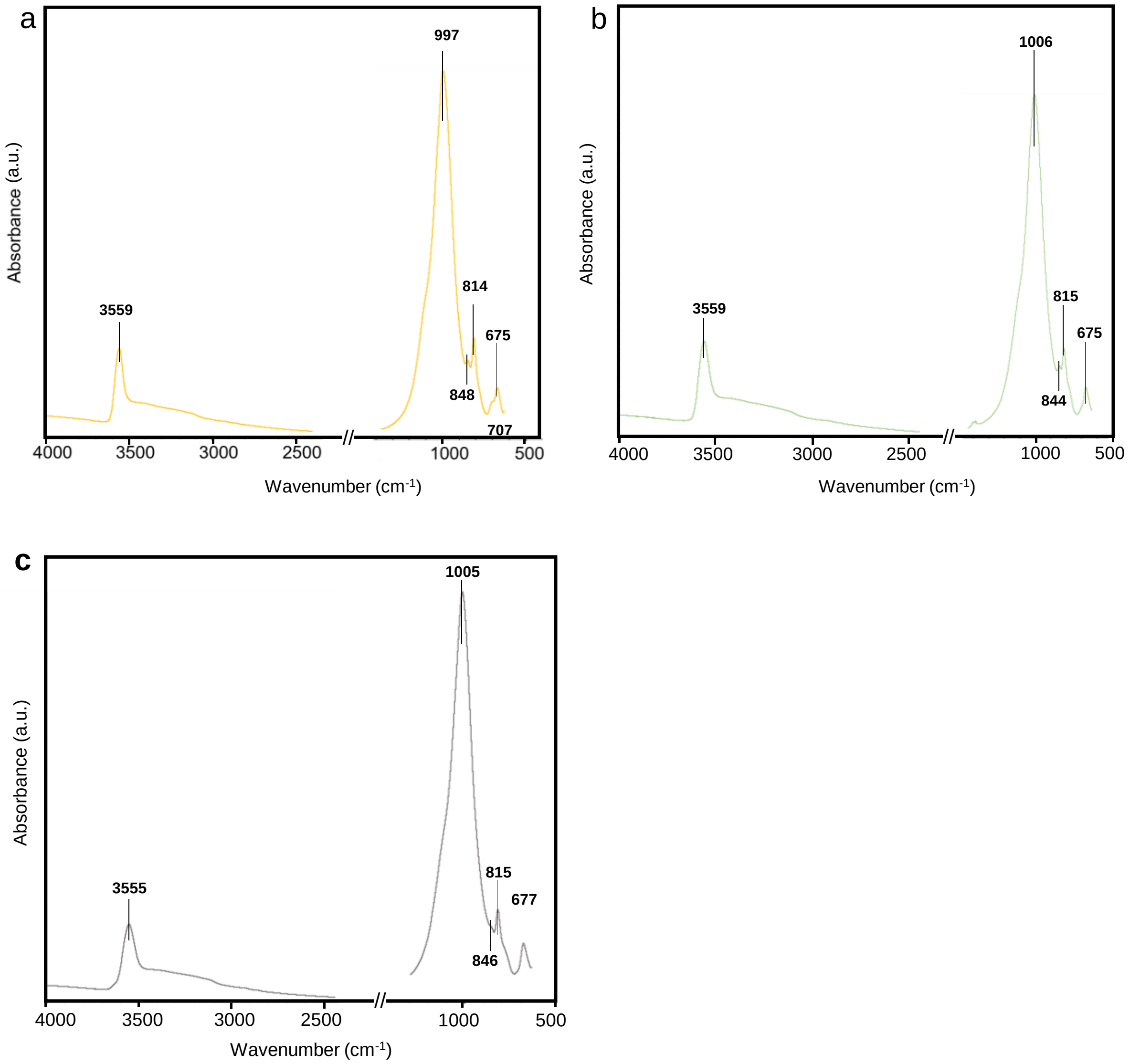

Figure S2: MIR Spectra of synthetic samples corresponding to Sm-HC (charge = 1.14) (a), Sm-LC (charge = 0.66) (b) and Sm-Mg (charge = 1.38) (c).

The vibrations at 3560 cm^{-1}, 816 cm^{-1} and 845 cm^{-1} are characteristic of di-octahedral environment. The stretching νFe^{3+}-OH-Fe^{3+} vibration and the bending δFe^{3+}-OH-Fe^{3+} vibration correspond to the 3560 cm^{-1}and 816 cm^{-1} positions respectively. Also, the 845 cm^{-1} band was usually observed for nontronite. The bands in 1000 cm^{-1} region correspond to the νSi-O vibration. This vibration shifts toward higher wavenumbers as amount of Fe(III) for Si(IV) substitutions increases. The 677 cm^{-1} and 707 cm^{-1} bands are also linked in part to the amount of tetrahedral Fe(III). Intensity of 707 cm^{-1} band increases as the amount of tetrahedral Fe increases. So, the band was displayed on Sm-HC spectrum but was not visible on Sm-Mg and Sm-LC spectra as a result of lower amount of tetrahedral Fe(III) in these two structures. The low content of Mg in Sm-Mg sample not allowed to observe bands involving Mg.

1.2. X-ray diffraction analysis

The oriented preparation was used to analyze the synthetic clays to ensure the expression of reflections corresponding to the 001 plan. The diluted suspensions of synthetic Na-saturated samples were placed on a glass slide; so, clays were oriented according to their c-axis.

The XRD patterns of oriented preparations of initial minerals in the air-dried (AD) conditions, and after the ethylene-glycol (EG) solvation were recorded using a Bruker D8 advance diffractometer (CuKα, 40 kV, 40 mA). The XRD patterns were obtained using a step size of 0.025°2θ over the 2-35°2θ range and a counting time of 0.6 s as acquisition conditions.

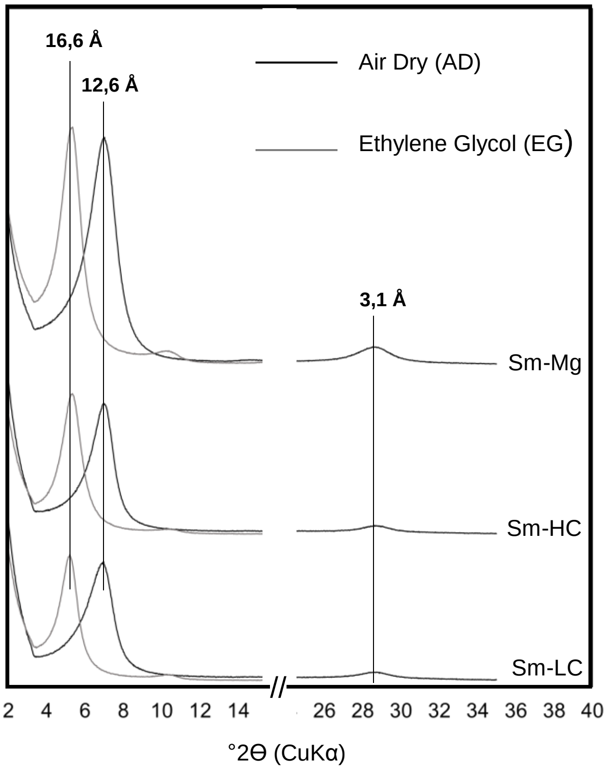

Figure S3: XRD patterns recorded for the oriented preparations of synthetic samples after Na saturation. Patterns recorded in air-dry (AD) and after ethylene-glycol solvatation (EG) are represented by black line and grey line, respectively.

The oriented preparation of the three synthetic samples exhibited a 001 reflection at 12.6 Å and a 004 reflection at 3.1 Å in air-dry (AD) condition. These two reflections were rational and the apparent 001 distance indicated that most of the layers were in mono-hydrated state. No other crystalline phases were detected. After ethylene-glycol (EG) solvation, the XRD patterns of Na-saturated samples exhibited a d_{001} of 16.6 Å, which corresponds to two layers of EG molecules. All observations confirm the synthesis of minerals with a smectitic behavior.

1.3. Thermodynamic constants

An equilibrium constant was associated with each dissolution equation for Fe(III)-rich smectites. The equilibrium constants were determined using a computer tool (ClayTherm) developed by Blanc et al. (2021). This tool is dedicated to estimating the thermodynamic properties of anhydrous and hydrated clay minerals. It combines several previously published estimation models (Blanc et al., 2015; Gailhanou et al., 2017; Vieillard et al., 2019) and is used to predict equilibrium constants for clay minerals and to compare the calculated thermodynamic properties with solubility data selected from the literature. It is based on a combination of determination of anhydrous (Enthalpy, enthropy and heat capacity), hydration (enthalpy and enthropy of hydration reactions) and bulk water thermodynamic properties. The model for entropy and heat capacity estimation is based on a method of decomposition in polyhedral units, while it is based on the electronegativity scale for enthalpy.

2. Experiments performed with the synthetic Fe(III)-rich smectites.

A total of 15 flow experiments were carried out with Fe(III)-rich synthetic smectites. Additional experiments were carried out to assess the reproducibility of the results obtained from the two reactors.

Table S2: Experimental conditions and results of flow-through dissolution experiments at steady state.

Experiment ‡	**Mass (mg)**	**Flow rate $(mL.s^{-1}).10^{-3}$**	**SS days**	**pe output**	**pH input**	**pH output**	**[Si] µM**	**[Fe] µM**	**[Mg] µM**	**Log R_{Si}**	**Log R_{Fe}**	**ΔG $kcal.mol^{-1}$**
Sm-HC-1.8-A	40	1.08	12	13.5	1.85	1.87	83.47	53.53		-9.17	-9.09	--5.05
Sm-LC-1.8-A	40	1.05	17	13.6	1.85	1.90	67.24	41.50		-9.34	-9.26	-5.24
Sm-LC-1.8-B	40	0.77	13	13.7	1.80	1.84	85.08	56.58		-9.40		
Sm-Mg-1.8-A	40	1.01	14	13.7	1.82	1.87	83.78	51.43	5.25	-9.23	-9.05	-16.02
Sm-HC-2-A	30	1.08	10	13.5	2.04	2.08	37.16	24.93		-9.59	-9.63	
Sm-HC-2-B	30	0.73	14	13.3	2.01	2.06	63.14	43.05		-9.58	-9.69	-3.74
Sm-LC-2-A	30	1.06	12	13.3	2.04	2.08	14.38	7.71		-10.12	-10.21	-9.14
Sm-Mg-2-A	40	1.09	10	13.7	2.01	2.08	64.61	38.43	6.56	-9.48	-9.43	-14.81
Sm-HC-3-A	40	1.06	19	11.9	3.03	2.95	4.57	1.15		-10.72	-	-7.57
Sm-HC-3-B	40	0.75	24	12	3.03	2.97	6.72			-10.71	-	
Sm-LC-3-A	40	1.09	31	12.3	3.03	2.93	3.93	1.38		-10.80	-	-7.84
Sm-Mg-3-A	45	1.13	18	12.1	2.96	2.91	6.05	1.12	0.48	-10.65	-	-18.47
Sm-HC-4-A	45	1.08	19	10.8	4.00	3.91	3.65	0.02*		-10.88	-	-6.78
Sm-LC-4-A	45	1.11	30	11.2	4.00	3.96	2.99	0.03*		-10.96	-	-7.36
Sm-Mg-4-B	60	0.76	16	10.2	4.01	4.08	5.69	0.02*	0.15	-11.00	-	-17.03
Sm-Mg-4-A	45	1.10	18	10.2	4.01	4.06	3.15			-10.96		
Sm-HC-5-B	70	1.09	21	9.4	5.4	5.48	1.55	bdl		-11.45	-	-1.81
Sm-LC-5-B	85	0.79	28	9.4	5.49	5.31	2.26	bdl		-11.54	-	-3.96
Sm-Mg-5-B	85	0.75	20	8.5	5.49	5.32	2.51	bdl	0.05	-11.51	-	-13.19

‡ Labels indicate: Sm = smectite; HC = high charge; LC = low charge, Mg = magnesium; 1.8, 2 ,3, 4, 5 = pH; A = reactor type A, B = reactor type B.
SS: days from the beginning of the experiment to steady state.
pe: redox potential
***Semi quantitative concentrations measured between limit of quantification and limit of detection (LD_{Fe} and LD_{Mg} = 0.01 µM).**
bdl: below detection limit.

3. Output solution analysis: experiments performed at pH 4 and pH 5.5 with Sm-HC and Sm-Mg.

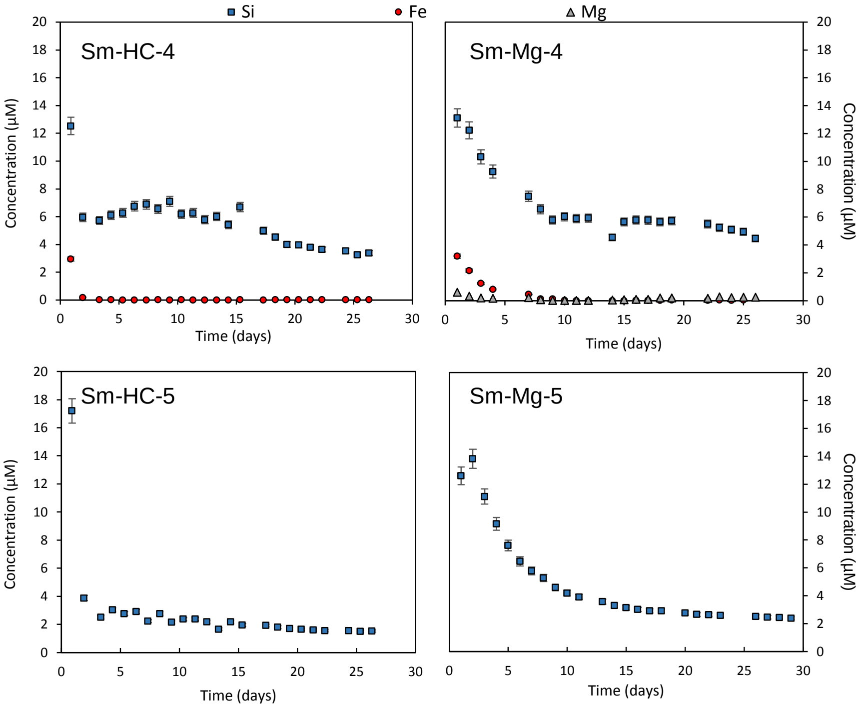

Figure S4: Evolution of Si, Fe, and Mg aqueous concentrations, measured as a function of time in the output solutions for dissolution experiments performed at pH 4 and 5.5 with Sm-HC and Sm-Mg. Concentrations of Fe and Mg are below quantification limits (1.27 µM and 0.5 µM respectively).

4. Saturation indexes of the output solutions

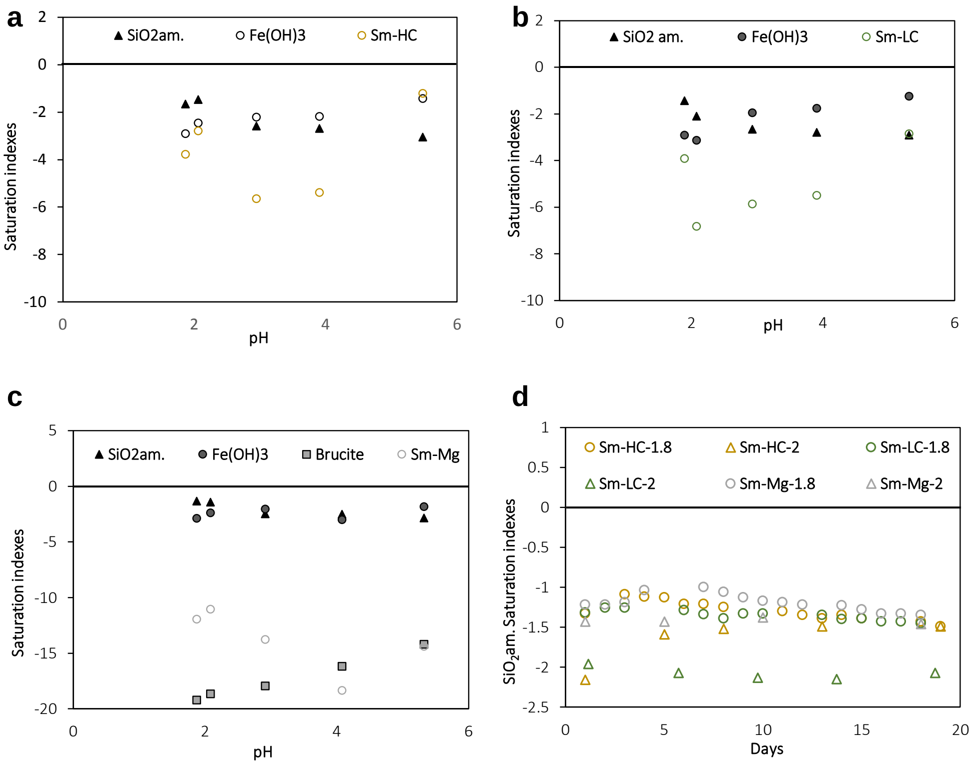

Figure S5: Variation with pH of the saturation indexes of the output solutions obtained at the stationary state for experiments performed with (a) Sm-HC (b) Sm-LC and (c) Sm-Mg. Variation with time of saturation indexes of output solutions relative to amorphous silica for experiments carried out with the three synthetic clay minerals and performed at pH 1.8 and pH 2 (d).

Saturation indexes of the output solutions with respect to amorphous silica, Fe ($Fe(OH)_3$) and Mg (Brucite) -bearing phases and each synthetic smectite were determined at steady sate for each pH condition (Fig. S4 a, b, c). Iron oxide $Fe(OH)_3$ was chosen as Fe-bearing phase due to their highest instability among the iron oxyhydroxides available in Thermoddem database. Saturation indexes of the output solutions with respect to the amorphous silica were determined in function of time for experiments performed at pH 1.8 and 2 (Fig. S4d), to control the solution saturation when the Si concentration measured in output solution was maximal. Throughout the experiments, output solutions were always undersaturated with respect to these phases.

5. FTIR spectroscopy analysis of dissolved Fe(III)-rich smectites

Table S3: Positions of 𝜈Si-O and 𝜈OH bands and relative intensities of [4]Fe(III)-O, 1100 cm-1, and 3150 cm-1 bands for initial and altered synthetic Fe(III)-rich smectites samples at various pH values.

Samples	**𝜈Si-O**	**𝜈OH**	**$^{[4]}$Fe(III)-O**	**1100 cm^{-1}**	**3150 cm^{-1}**
Sm-HC	997	3559	++++	ABS	-
Sm-HC-5	1003	3561	+++	ABS	-
Sm-HC-4	1005	3566	+++	ABS	-

Sm-HC-3	1004	3563	++	ABS	+
Sm-HC-2	1004	3565	+	ABS	++++
Sm-HC-1,8	1010	3567	+	+++	+++
Sm-LC	1006	3559	-	ABS	-
Sm-LC-5	1004	3560	-	ABS	+
Sm-LC-4	1008	3564	-	ABS	+
Sm-LC-3	1008	3565	-	ABS	+
Sm-LC-2	1008	3567	-	ABS	+++
Sm-LC-1,8	1012	3568	-	ABS	++
Sm-Mg	1005	3555	ABS	ABS	-
Sm-Mg-5	1010	3558	ABS	ABS	-
Sm-Mg-4	1009	3558	ABS	ABS	-
Sm-Mg-3	1010	3558	ABS	ABS	-
Sm-Mg-2	1012	3562	ABS	ABS	++++
Sm-Mg-1,8	1015	3563	ABS	+++	+++

ABS: band is not present on the spectrum.

6. Morphological and crystal chemical evolutions of Fe(III)-rich particles observed by (HR)TEM analysis

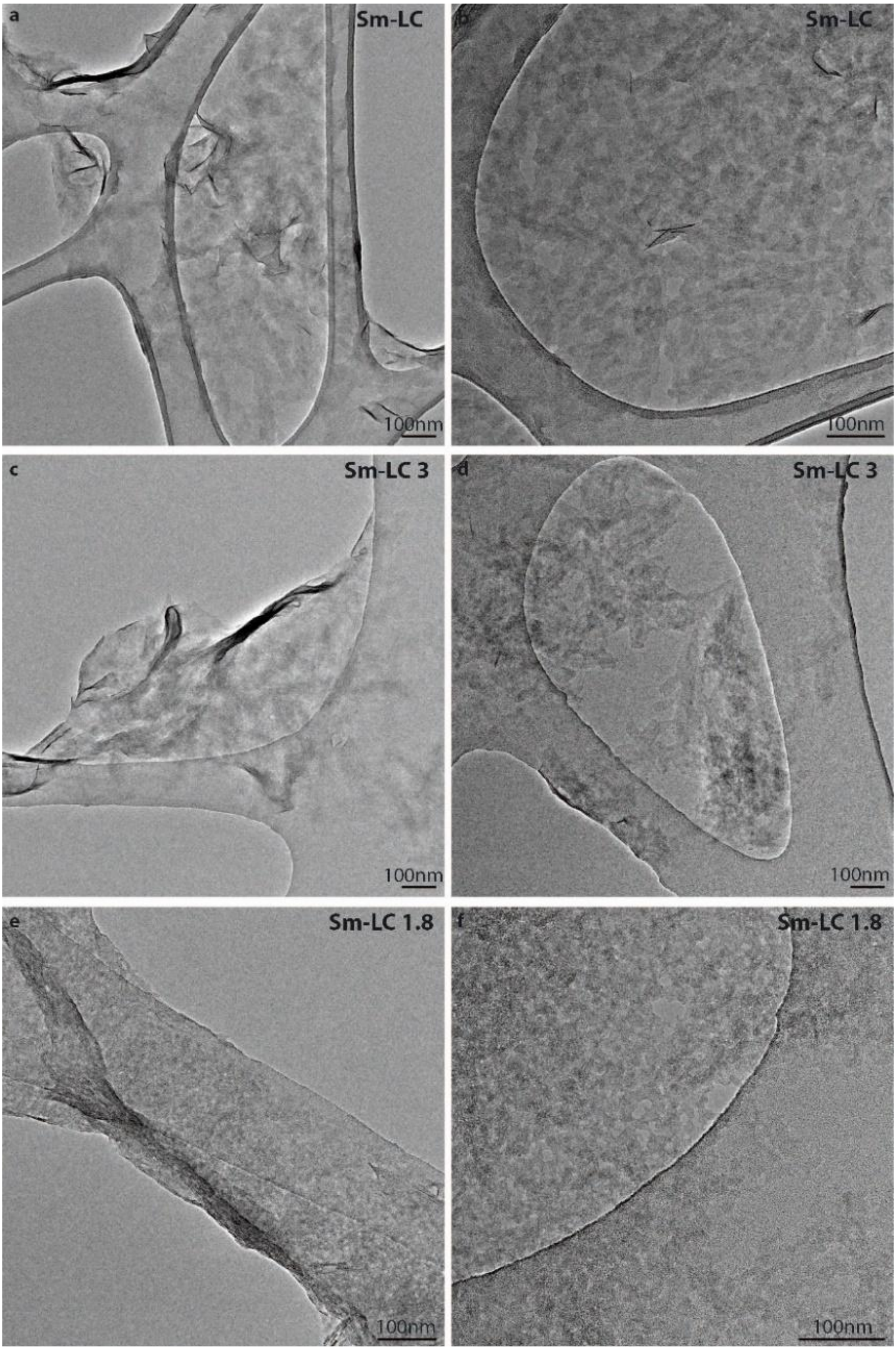

Figure S6: TEM Observations of initial Sm-LC particles (a, b) and of Sm-LC particles altered at pH 3 (c, d) and 1.8 (e, f).

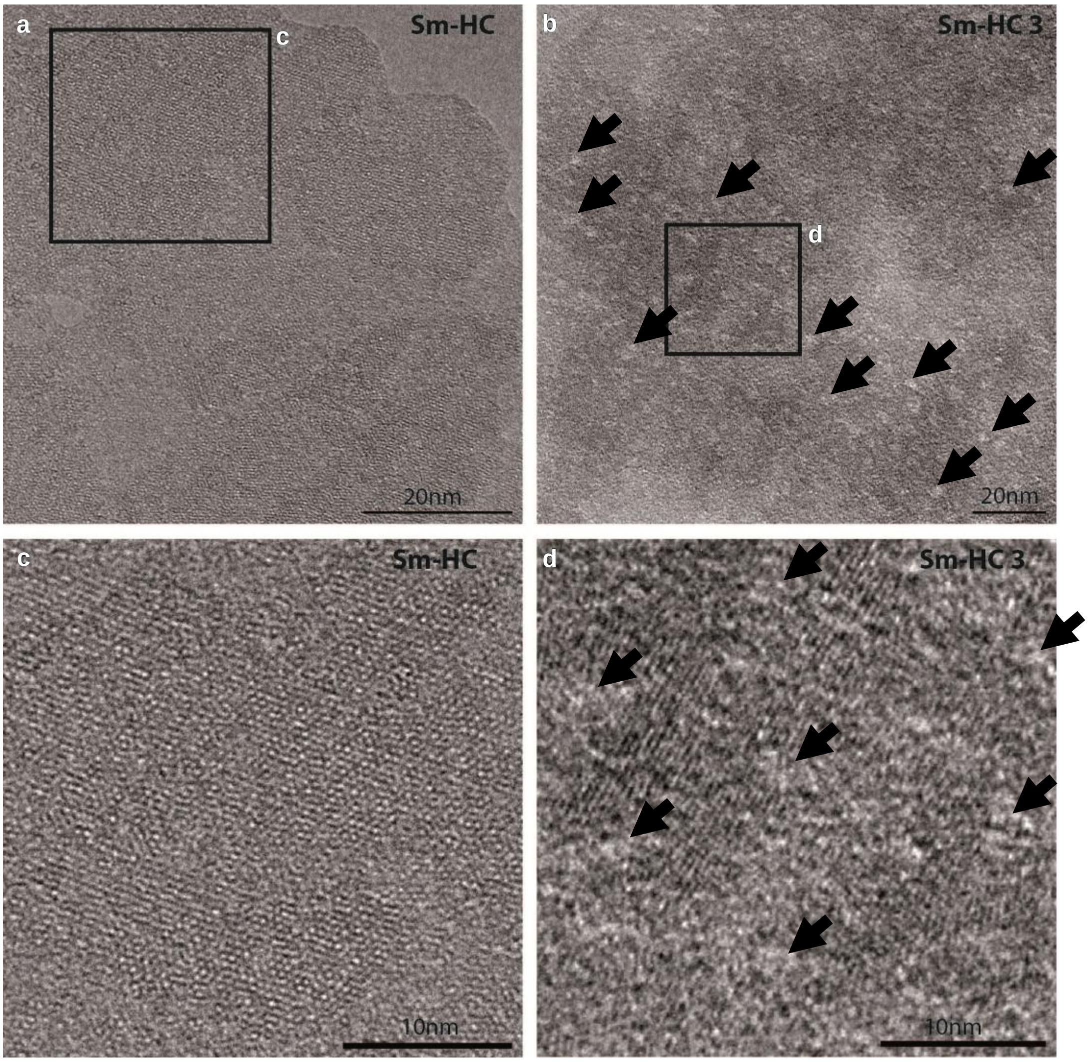

Figure S7: HRTEM Observations of (a) initial Sm-HC particles, (b) altered Sm-HC particles at pH 3, (c) zoom on the structure of Sm-HC initial particles, and (d) zoom on the structure of Sm-HC particles altered at pH 3. Arrows point at the zones were amorphization is observed (loss of well-arranged atomic structure), corresponding to whitish spots on figure (b).

7. Properties of natural smectites mentioned in this study

Table S4: Details relative to the structural formula of the natural smectites taken from the literature.

Structural formulas of Natural Fe(III)-rich smectite	**Global charge (per $O_{20}(OH)_4$)**	**Nature and % tetrahedral charge**	**Nature and % octahedral charge**	**Tetrahedral Si/Fe ratio**	**Global Si/Fe ratio**
NAu-1 $(Si_{6.98}Al_{1.02})(Al_{0.29}Fe_{3.68}Mg_{0.04})O_{20}(OH)_4M^+_{1.06}$ (Gainey et al., 2014)	1.06	Al (III) → Si 96	Mg → Fe (III) 4		1.89
Structural formulas of Natural Al-rich smectites					
SBId1 $(Si_{7.148}Al_{0.852})(Al_{3.624}Fe_{0.224}Mg_{0.18})O_{20}(OH)_4M^+_{0.948}$ (Robin et al., 2016)	0.95	Al (III) → Si 90	Mg → Al (III) 10		31.9
FEBEX $(Si_{7.82}Al_{0.18})(Al_{2.9}Fe_{0.36}Mg_{0.88})O_{20}(OH)_4M^+_{0.68}$ (Cappelli et al., 2018)	0.68	Al (III) → Si 26.5	Mg → Al (III) 73.5		21.7
SAz-1 $(Si_{7.70}Al_{0.30})(Al_{2.77}Fe_{0.17}Mg_{1.11})O_{20}(OH)_4M^+_{1.25}$ (Amram and Ganor, 2005)	1.25	Al (III) → Si 24	Mg → Al (III) 76		45.3

8. Data from studies used to calculate the Gibbs free energies for dissolution of natural smectites

Data related to the dissolution of FEBEX smectite were directly extracted from Cappelli et al. (2018) study.

Natural Smectites	**Beidellite SBId1** **Robin et al., 2015**	**Nontronite NAu-1** **Gainey et al., 2014**
Dissolution equations	$(Fe_{0.224}Si_{7.148}Al_{4.476}Mg_{0.18}O_{20}(OH)_4)^{-0.948} + 15.408H^+ + 4.592H_2O = 0.224Fe^{3+} + 4.476Al^{3+} + 0.18Mg^{2+} + 7.148H_4SiO_4$	$(Fe_{3.68}Si_{6.98}Al_{1.31}Mg_{0.04}O_{20}(OH)_4)^{-1.03} + 16.08H^+ + 3.92H_2O = 3.68Fe^{3+} + 1.31Al^{3+} + 0.04Mg^{2+} + 6.98H_4SiO_4$
Log $K_{(25°C)}$*	7.58	-4.05
[Si] mM	$9.86.10^{-3}$, $4.56.10^{-3}$, $3.20.10^{-3}$	3.248, 0.830, 0.315
[Al] mM	$7.08.10^{-3}$, $3,74.10^{-3}$, $1.90.10^{-3}$	0.752, 0.573, LD‡
[Mg] mM	LD‡, LD‡, LD‡	0.01, 0.01, 0.18
pH	1.07, 1.85, 2.77	1.10, 1.88, 3.62

Table S5: Data related to the dissolution of SBId1 and Nau-1 at 25°C

* The equilibrium constants for the natural smectites were computed following the method proposed by Blanc et al. (2021).

‡ LD=limit detection: when the concentrations of elements were not available in the study, the detection limit values were used.